State-dependent circuit dynamics of superficial and deep CA1 pyramidal cells in macaques

S. Abbaspoor[1], and K.L. Hoffman[1,2]

Affiliations:

[1] Department of Psychology, Vanderbilt Vision Research Center, Vanderbilt Brain Institute, Vanderbilt University, Nashville, Tennessee [2] Department of Biomedical Engineering, Vanderbilt University, Nashville, Tennessee

Abstract:

Diverse neuron classes in hippocampal CA1 have been identified through their heterogeneity in cellular/molecular composition. How these classes relate to the hippocampal function and network dynamics that support cognition in primates remains unclear. Here we report functional cell groups in CA1 of freely-behaving macaques that show a range of spectral phase preferences and varied responses to local network states like the sharp-wave ripple. Segregating superficial- from deep-layer pyramidal cells uncovered differences in firing rate, burstiness, and sharp-wave ripple associated firing. They also showed strata-specific interactions with the inhibitory cell groups. CA1 ensemble recordings revealed the first observations of cell assemblies in the macaque hippocampus, and show that the stratification of pyramidal cells in primates is a major organizing principle of assemblies. These results suggest a sublayer-specific circuit organization in hippocampal CA1 of the freely-behaving macaque that may support dissociable contributions across cognitive and behavioral processes in the primate.

Introduction

Circuit dynamics specific to the hippocampus govern its role in navigation, memory, and social/motivational behaviors across species[1–7]. Based on studies in rats and mice, these dynamics arise from a well-described and diverse range of cell classes[8–11]. For example, the pyramidal cell layer is organized into radial-axis strata[12], each receiving distinct afferents[13–16], bearing different intrinsic and task-related response characteristics[15,17–23], and projecting to different target structures[12,22]. The dynamics of these pyramidal cells are precisely regulated by inhibitory cell classes[10,24,25] that differ from each other in their behaviorally-specific firing patterns and roles in shaping network oscillations[11,26–30]. Because these cell classes differently segregate pyramidal cell assembly patterns in space and time[29,31,32] they may be fundamental determinants of the role of these assemblies in memory and navigation.

Although many aspects of hippocampal physiology are conserved between rodents and primates, differences in oscillatory dynamics[33–38] and behavior-specific modulation[39–44] suggest there may be phylogenetic specializations that an understanding of the underlying functional cell composition may uncover. A first-pass bisection of hippocampal (and medial temporal lobe) cells in primates into putative inhibitory and excitatory classes (or four groups[45]) reveals characteristic responses at both the circuit-level[35,46,47] and cognitive/behavioral levels[48,49]. Beyond that coarse division, we lack a description of primate CA1 functional cell types, that can bridge what is known from anatomy and rodent physiology to circuit function and behavior. To gain a better understanding of the degree of functional conservation in the hippocampal CA1 region, we sought to identify potential functional cell types, delineating their characteristic laminar and spectral profiles during active wakefulness and sleep. Additionally, we describe CA1 pyramidal cell activity in primates along their previously-unexplored superficial and deep strata, including basic physiological responses, pairwise activity among the pyramidal groups and relative to putative inhibitory cell groups, and finally, in relation to network properties including oscillations and synchronized assemblies of activity.

Results:

Identification of functional cell groups in laminar recordings of macaque CA1

We recorded from hippocampal CA1 layers in two freely-behaving macaques, as they performed a sequential memory task and during rest/sleep (Figure 1, A and B). Across 35 daily sessions (M1: 17 sessions, M2: 18 sessions) we measured the local field potentials and activity in ensembles of units. To align recording depths across these sessions and animals, we calculated for each session the current source density (CSD) during sharp-wave ripple (SWR) events. SWRs are known to evoke sinks in the Stratum Radiatum and sources in the Stratum Pyramidale layers of CA1[50] (Figure 1C). Within this region, we found the slope of the slow component of sharp-wave ripples, which crossed zero across all sessions and animals, and we aligned to that zero-crossing. To validate that alignment, we measured ripple power, which peaks within the central region of the pyramidal layer (Figure 1C). After identifying single unit activity typically consisting of waveforms across several adjacent channels (Figure 1B), we selected the electrode contact with the largest spike amplitude for each unit as the best estimate of the location of the cell body. This reduced some of the known within-cell variability in waveshape. The regular linear distribution of these recording sites on the probe shanks allowed us to determine the relative depths of the cell bodies of the simultaneously-recorded neurons (Figure 1D).

We classified various cell groups with a semi-supervised approach according to their normalized waveform [51,52] and their interspike interval (ISI) distributions, to capture several of the principal intrinsic physiological characteristics that differ by cell type. This led to 10 separate cell groups (Figure 1D, see Methods; overall between-group distances exceeded within-group distances: $p < 0.001$, Kruskal-Wallis, Figure S1A). We use the term "cell groups" throughout to refer to these 10 clusters, and note that these groups are clustered based on extracellular physiological features only, and thus may differ from the formal "cell classes" or "cell types" as identified through molecular/immunohistochemical methods or cytoarchitectonics.

The incorporation of the ISI distributions as features along with spike waveforms, qualitatively drew out cells with bursting activity, low-firing rates, and broad waveforms, characteristic of pyramidal cells[53,54]. These comprised the first cell group (Figure 1D, far left, black, notably well-localized to the ripple layer i.e. Stratum Pyramidale). The other negative-deflecting groups were therefore considered putative inhibitory cells, because pyramidal cells are the only excitatory cell class in CA1. As expected from these features, firing rates of these cell groups differed ($p<0.001$, Kruskal-Wallis, Fig. 1D, Figure 1D and S1C inset); and in addition, 3 neuron types selectively decreased firing during sleep compared to waking behavior ($p<0.001$, permutation test, Figure S1B). The ISI-conditioned coefficient of variation, CV2, measures the intrinsic variability of local spiking intervals, irrespective of global firing rate changes like those seen across behavioral epochs[55]. As expected, cell groups also showed differences in CV2 ($p<0.01$, Kruskal-Wallis test with post-hoc permutation test FDR corrected, Figure S1C), leading to distinct, cell group-characteristic joint ISI histograms (Figure S1D).

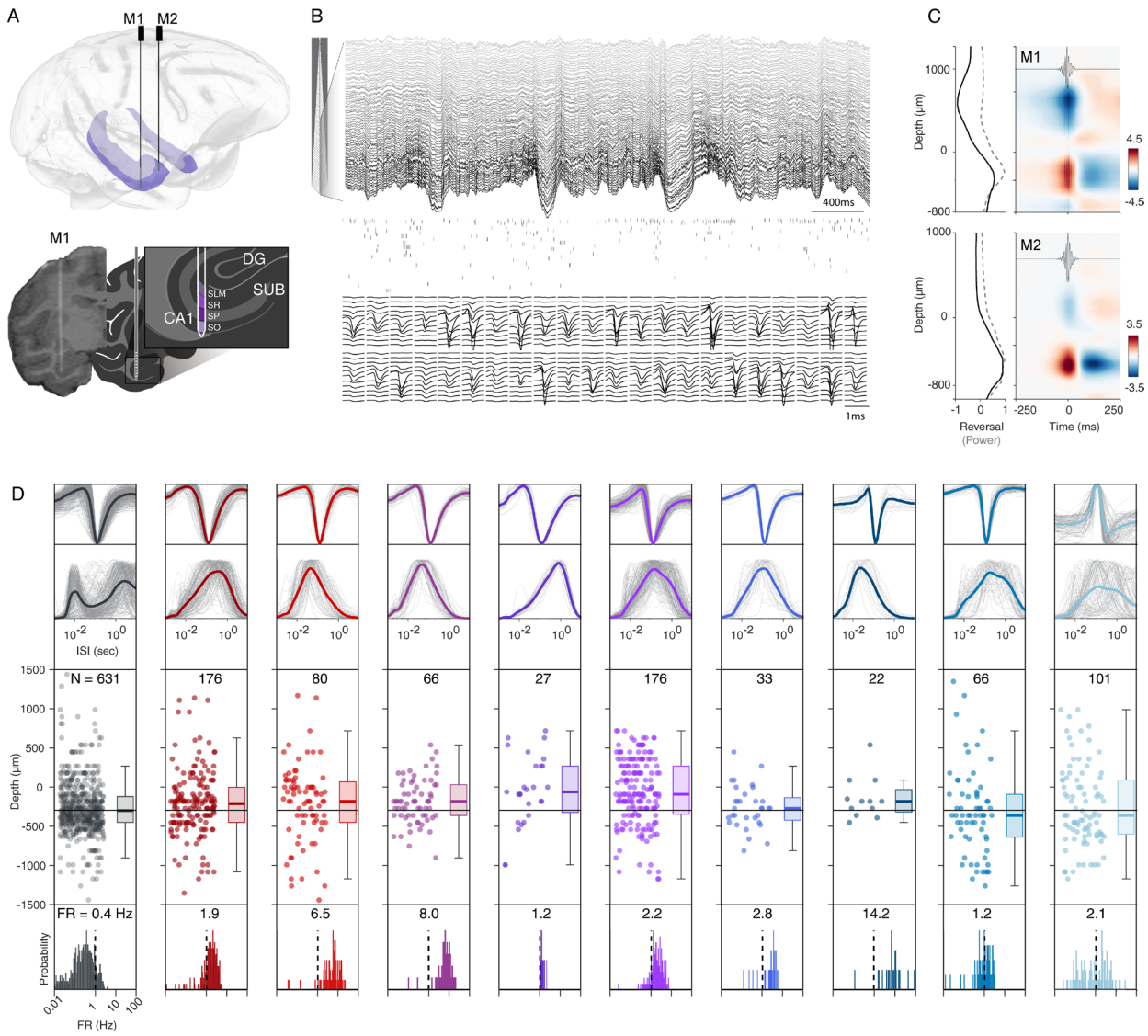

Figure 1. Single units from macaque CA1 characterized by depth and physiological parameters. (A) Top: schematic rendering of the electrode arrays localized to the target regions for each animal (M1, M2), in anterior hippocampal CA1. Dark purple: CA1. Both animals' trajectories were localized with CT-MR registration and verified physiologically. Bottom: Coronal view of the CT coregistered to MR for one electrode trajectory, targeting the hippocampal CA1, and schematic of hippocampal CA1 layers. **(B)** Top: LFP traces across 64 of 128 recorded channels of one probe (40 micron spacing) spanning layers of hippocampal CA1. Middle: Spike raster of simultaneously recorded neurons from this probe (N = 48). Bottom: Example spike waveforms for selected units from this recording. **(C)** Top, left: Ripple slope reversal (black) and ripple power (dashed gray) across channels (depth). Top, right: Current source density of average ripple LFP for monkey 1 (blue: sink, red: source). Bottom: The same as top but for the 2nd animal. **(D)** CA1 cell groups. 1st Row: Grand mean (colored) and unit-mean (gray) waveforms (1.5 ms) for each cell group. 2nd Row: Grand mean (colored) and unit-mean (gray) log interspike-interval distributions (0-10 s) for each cell group. 3rd Row: Estimated depth of units aligned to ripple reversal (0 µm). Box plots (throughout) show median and quartiles. Depths differed by group, $p < 0.001$, Kruskal-Wallis test. Superficial-deep pyramidal split shown by black horizontal line (-330 µm). N= number of units per group. 4th Row: Distribution of mean firing rates, shown for each cell group, dashed line at 1 Hz. Grand mean reported at top of plot. Firing rates differed by group, ($p < 0.001$, Kruskal-Wallis test).

Spectrolaminar profiles and spike-phase coupling by cell group

To better understand oscillatory composition across layers, we computed aperiodic-corrected power spectra (Figure 2A). Despite inter-subject differences in absolute peak frequencies across the spectrum, both subjects showed reduced theta-band power (5-10 Hz) during active wakefulness in comparison to rest or early sleep overnight, across all recorded channels ($p<0.05$, cluster-based permutation test, Figure 2A), in line with previous studies[33–35]. Furthermore, in the pyramidal layer, the active wakeful states showed relative increases in power in the mid frequencies of 15-40 Hz (Figure 2A), and each animal had a preferred higher gamma band apparent during active waking (Figure S2A). These general profiles were also evident in the spike-phase coupling across units, measured as the pairwise phase consistency (PPC; Figure 2B and S2B). Comparing across states, spike-field coherence within the theta frequency range (5-10 Hz) was greater during sleep ($p<0.05$, two-sample permutation test) seen across all cell groups (Figure S2B). Conversely, spike-field coherence in the slow (25-35 Hz) and higher (50-75 Hz) gamma ranges were significantly higher during wakefulness ($p<0.05$, two-sample permutation test, Figure 2B), across cell groups.

Focusing only within band-limited bouts of high power, cells showed a generally large bandwidth, showing significant phase-locking to, on average, 4.4 of the 8 frequency bands. The grand mean phase angle per cell group revealed that these groups typically clustered within a limited range of preferred phases (~90 degrees) that shifted by frequency (Figure 2C and S2C), but nevertheless differed reliably in mean phase-of-firing values for all but the lowest frequencies (except for 1-4 Hz, 4-7 Hz, and 7-13 Hz, $p < 0.001$, multi-sample Watson-Williams test, Figure S2C). Using the pyramidal cell group as a reference, the other cell groups deviated in phase angle as function of frequency and cell group (Figure S2C-D; $p < 0.05$, two-sample Watson-Williams). Among cells exhibiting significant phase locking ($p<0.001$, Rayleigh test) within each frequency group, the largest resultant vectors were found in the following order: 1-4 Hz, (100-180 Hz and 4-7 Hz), 60-90 Hz, (30-60 Hz and 20-30 Hz), (7-13 Hz and 13-20 Hz) ($p<0.05$, Kruskal–Wallis test with Tukey-Kramer correction); therefore the power spectral peaks were not necessarily those yielding the strongest phase-locking during band-limited bouts.

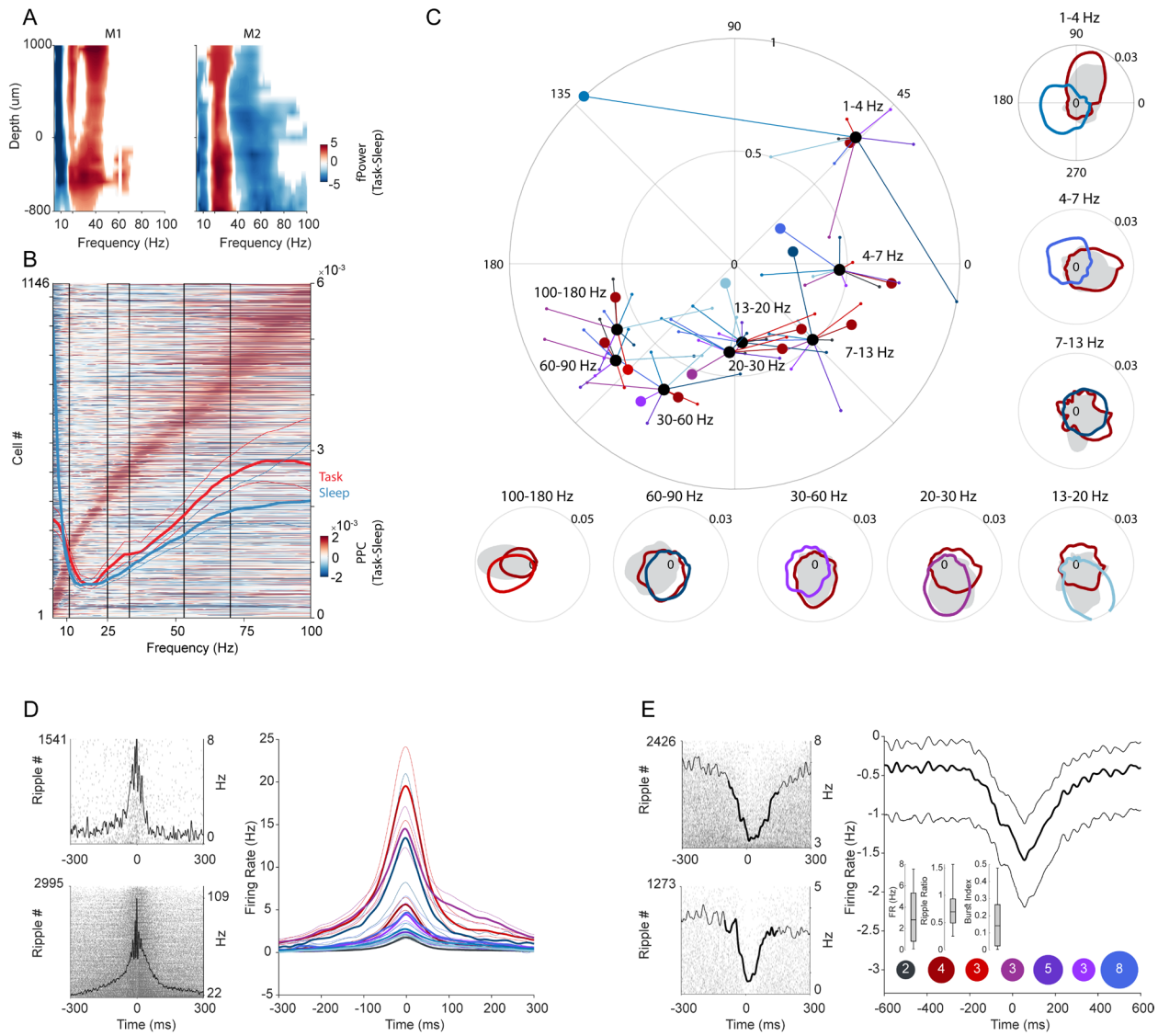

Figure 2. Local field potential dynamics and spike-field relationships across cell groups. (A) Spectrolaminar differences by behavioral state for each animal. Left: Color difference plot of 1/f corrected power spectrum of alert, task-related (red) and rest/sleep states (blue) across depths of recordings for monkey 1. Non-significant differences by state are masked in white (significance set to $p < 0.05$, cluster-based permutation test) Right: Results for monkey 2 using the same conventions as for Monkey 1. **(B)** Pairwise phase consistency (PPC) differences between task and rest/sleep states per unit, sorted based on each unit's maximum PPC frequency. Mean PPC (thick lines) and bootstrap 95% CI (thin lines) are shown for the task in red, and for rest/sleep in blue, with values shown on the right axis. Black boxes indicate those frequency ranges that differed across states ($p<0.05$, two-sample permutation test with Tmax multiple comparison correction). **(C)** Center, large: Phase-of-firing plot depicting the average resultant vector lengths and phase angles for each cell group, as a function of LFP frequency bands. Each color dot indicates the grand mean resultant vector length and angle for the respective cell group, plotted separately for each frequency band. Thick black dots represent the mean of those cell groups means, for each frequency band. Off-center, small: Phase-of-firing plots of selected single-neuron examples, organized according to LFP frequency bands. Examples are colored according to group membership; gray = group 1 putative pyramidal cells. **(D)** Peri-SWR enhanced unit responses. Left: Example raster and PETHs of individual neuron activity during ripple, and the superimposed line showing the mean response. Right: Lines show mean + bootstrap 95% CI for baseline-corrected ripple-associated activity for

ripple-activated neurons ($p < 0.05$, one-sample randomization test) separated and color-coded according to cell groups. **(E)** Peri-SWR suppressed unit responses. Left: Example rasters as in (D), with the time window of significant modulation indicated by the bold black line. Right: conventions as in (D), for all ripple-suppressed cells. Inset: Quantile distributions across cells are shown for firing rate, ripple ratio and burst index (see Methods). Colored circles indicate the group identities and count of cells comprising the suppressed population.

Cell type-specific ripple-associated activity

Most cells increased their firing during ripples, across all cell groups ($p<0.05$, one-sample randomization test, Figure 2D and 3A) though to differing degrees (ripple ratio, during/baseline FR,$p < 0.001$ Kruskal-Wallis test, Figure S3B), and with differences in participation rate across ripple events ($p<0.001$ Kruskal-Wallis test, Figure S3B). The pyramidal cell group showed the highest ripple ratios but the lowest participation rate ($p<0.001$, pairwise permutation test, FDR corrected, Figure S3B). Putative inhibitory cell groups showed a striking range of participation probability and timing: some groups' members participated in all ripple events (Figure S3B), and some restricted firing to a specific time relative to ripple peak (Figure S3B; $p < 0.001$, Bartlett's test). A small population of cells had suppressed activity during the ripple, and these were comprised mainly of the inhibitory (non-pyramidal) cell groups ($p < 0.05$, one-sample randomization test, Figure 2E).

Stratification into superficial and deep CA1 pyramidal cells reveals physiological heterogeneity

To extend findings from the rodent literature, we examined whether CA1 pyramidal cells recorded in different depths of Stratum Pyramidale differ in their spiking properties and circuit-level dynamics. For each session, cells in the 'Pyramidal' group (meeting firing rate and burst and depth criteria), were median split according to depth, creating the CA1sup group (closer to Stratum Radiatum) and the CA1deep group (closer to Stratum Oriens). Compared to CA1deep cells, the firing rates of CA1sup cells were higher overall and during ripples, and they had a greater CV2 ($P < 0.05$, permutation test; Figure 3A-3C, Figure S1C), though they were less 'bursty' than their deeper peers ($P < 0.001$, permutation test; Figure 3B).

To investigate whether these cells interact differently, either within their subgroups, or in their coupling with the inhibitory groups, we analyzed their pairwise co-firing statistics. We found that pyramidal cells of the same sublayer were more likely to fire together compared with cells of different sublayers (Figures 3D), and they showed differences in co-firing strength with several of the inhibitory cell groups ($p<0.001$, permutation test; Figure 3E). The finer-grained temporal dynamics revealed greater detail in these interactions: baseline-normalized cross-correlograms (CCGs) also showed preferential within-sublayer firing ($p<0.01$, two sample permutation test with Tmax correction, Figure 3D), and among the inhibitory groups, CA1sup and CA1deep differed in their lead/lag spike timing and strength ($p<0.01$, two sample permutation test with Tmax correction, Figure 3E). Finally, CA1sup and CA1deep cells have somewhat opposite timing interactions with the ripple-suppressed cells: for CA1deep cells, the interactions peak at 0 ms, when CA1sup cell interactions are near their nadir; CA1sup cells' peak is at approximately 7ms lag ($p<0.01$, two sample permutation test, Figure 3H).

During ripples, CA1sup had a higher participation probability and fired more than CA1deep ($p<0.01$ two sample permutation test, Figure 3G). Relative to pre-ripple firing, CA1sup cells fired more post-ripple compared to CA1deep ($p<0.05$ cluster-based permutation test, Figure 3F). Finally, CA1deep cells are more strongly locked to the ripples and fire at a slight but significant phase advance compared to CA1sup ($p<0.01$ permutation test,$p < 0.001$ Kuiper's test, Figure 3G).

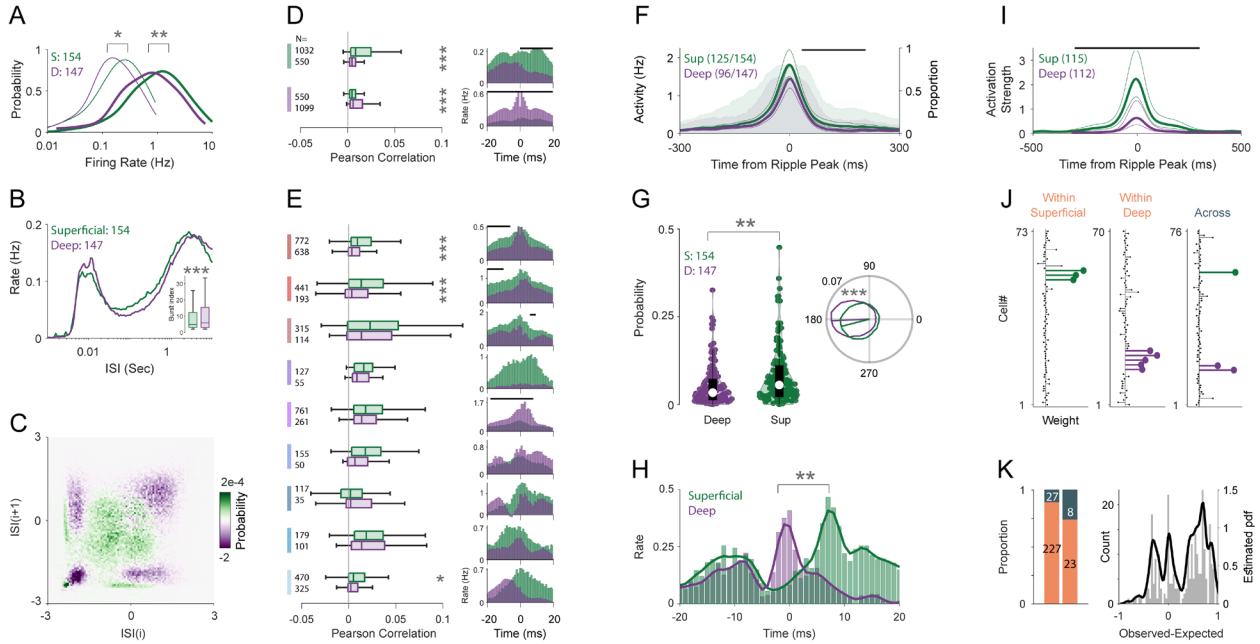

Figure 3. Sublayer-specific circuit dynamics of hippocampal pyramidal cells in macaque CA1. (A) Overall (thin lines) and ripple (thick lines) firing rate distribution for superficial (green, N= 154) and deep (purple, N= 147) pyramidal cells. **(B)** Mean ISI distribution. Inset: burst index distribution. **(C)** Difference (Sup-Deep) plot of joint probability density of current ISIs versus next ISIs. **(D)** Left: Pairwise cofiring of pyramidal cells with other pyramidal cells from within and across Sup, Deep groups. Referent group of pair shown by color code bar on the far left; target groups are Sup above (green), and Deep (purple), immediately below. Right: Mean cross-correlograms of sup/deep pyramidal cells. Black horizontal lines above plots (throughout) indicate significant difference ($p<0.05$, two-sample permutation test with Tmax multiple comparison correction). CCG values were baseline corrected (mean from -50 to -20 ms was subtracted from all bins). **(E)** Left: Pairwise cofiring of sup/deep pyramidal cells and putative inhibitory cell groups. Conventions as in (D). Mean cross-correlograms of sup/deep pyramidal cells and inhibitory cells. Conventions as in (D). **(F)** Ripple-aligned spike density (mean + 95% CI) for significantly modulated cells (N = 125 superficial, and 96 deep), black horizontal line shows significant differences ($p < 0.05$ cluster-based two-sided permutation tests). The proportion of significantly modulated units relative to the ripple peak is shown in the shaded area plots, units on the right axis ($p<0.05$, one-sample cluster-based permutation test). **(G)** Left: Distribution of the ripple participation probability. Right: Phase concentrations and mean resultant vector for significantly phase locked units (N = 74 superficial, 98 deep, p = 1e-3 Kuiper two-sample test/p=2e-4 permutation test). **(H)** Mean cross-correlograms of sup/deep pyramidal cells and ripple-suppressed inhibitory cells (N= 16 superficial, 20 deep,$p < 0.05$, two-sample permutation test with Tmax multiple comparison correction). **(I)** SWR-triggered average activation strength in post-task sleep for Deep (N = 115) and Sup (N = 112) cell assemblies. ($p<0.05$, two-sample cluster-based permutation test) **(J)** Example assembly weights for two "within" assemblies and one "across". Rows indicate cells, and their length indicates their weight in that assembly. Significant members are colored. **(K)** Left: Fraction of within (N =227, orange) and across (N=27, dark gray) assemblies for all sessions and assemblies (N = 254) and for balanced sessions where the number of recorded deep and superficial were equal and assemblies that had at least 2 significant pyramidal members (N = 31). Right: Difference between expected proportions of within/across and observed proportions (N = 254). For a, b, c, d, e, and g, P values were computed using a two-sided permutation test (N = 5000).

CA1 cell assembly membership by strata and cell group

We used unsupervised detection of recurrent co-activity to identify cell assemblies during sleep epochs, using established methodologies (Figure 3J and S4A, Methods). Assemblies that included pyramidal cell contributions were assigned to "within superficial," "within deep," or "across", based on the category membership of those pyramidal cells. Our findings revealed that "within CA1sup" assemblies exhibited significantly stronger activation during ripple events in comparison to "within CA1deep" assemblies ($p < 0.05$ cluster-based permutation test, Figure 3I). Furthermore, assembly membership depended on layer, with most having all members belonging to the same sublayer (Figures 3K). Importantly, these results held after accounting for the priors (the observed exceeded expected sampling distributions of eligible cells by layer), and when only considering assemblies detected during balanced sessions, where an equal number of CA1sup and CA1deep cells were recorded and assemblies had more than 2 significant pyramidal cell members (Figure 3K).

A cell's selectivity across assemblies can be defined as the inverse of its participation rate (the proportion of assemblies to which a neuron significantly contributed, divided by all detected assemblies in a session). The majority of cells demonstrated a propensity for participating in specific assemblies, with a mean participation rate of 7% (Figure S3A). Participation varied by cell group (Figure S3C, $p < 0.001$, Kruskal-Wallis test and $p < 0.05$; post-hoc pairwise permutation test with FDR correction), and although there was an overall negative correlation between the firing rate of neurons and their participation rate ($p < 0.001$, t-test Figure S3D), firing rate could not completely account for participation by cell group.

Discussion:

Currently, any detailed microcircuit mechanism of the primate hippocampus thought to underlie its cognitive and behavioral functions must be extrapolated from the hippocampus of rodents. In this study, we sought to forge a link between the extensive understanding of CA1 microcircuit function from rats and mice[56] to the network dynamics and brain-behavior states seen during naturalistic experiences in primates. To accomplish this, we recorded in vivo, in freely-moving monkeys during species-typical behaviors. To this we added high-density laminar recordings that identified depth-localized populations of isolated single units fully embedded in their network context. Physiologically-defined pyramidal cells were concentrated in the SWR CSD source layer, and additional cell groups arose from the unsupervised clustering of waveform and ISI distribution, building on previous work[51,52]. The novel addition of the ISI distribution had the advantage of incorporating features that human experts often use in evaluating cell firing characteristics. In addition, it allowed for the full ISI range to inform the clustering, as opposed to thresholding into discrete burst/non-burst groups. The inclusion of ISI may help mitigate some potential limitations of using single-channel waveshape as a sole grouping criterion, such as extracellular waveshape variance due to different positions relative to the cell soma[57,58], and differences in absolute waveshape that may arise across preparations due to differences in electrochemical and physical properties of the recording electrode and of acquisition filter characteristics.

Here, we describe in the primate hippocampus a spectrum of 10 identified cell groups that constrain the CA1 microcircuit through i. their intrinsic firing characteristics, ii. their different engagement with pyramidal cells, iii. their firing prevalence and temporal organization relative to local field fluctuations, and to some degree, iv. their distribution in depth. Mesoscopic CA1-population/hippocampal spectrotemporal activity shows considerable differences in macaques relative to rats and mice[33,35,59–61]. For example, some aspects of gamma and sharp-wave ripples appear well conserved across species, whereas the multiple

circuit mechanisms driving hippocampal theta-band oscillations in rats and mice have yet to be dissected in primates. Conversely, the rodent circuits that could generate the equivalent to the hippocampo-cortical alpha or beta band, and their gamma coupling, as seen in monkeys[35,61,62], is yet to be firmly established in rodents (though see[63–65]). Our finding of wide bandwidths of spike-field locking among the cell groups of CA1 suggests that in general, cells have the flexibility to participate in a wide range of frequencies. Within this range, three specializations were nevertheless evident. First, cell groups' peak beta/gamma frequencies tiled the range of these frequencies (Figure S2B). Second, spike-phase timing in the weaker, mid-band frequencies of 7-30 Hz spanned the greatest range of phases (~90°) and exhibited the most groups with firing phases different from the pyramidal cells' phase (Figure S2C). Third, groups differed in their assembly participation, and this was not merely a function of firing rate (Figure S4C). These differences constrain the available functional space in primate CA1, which was previously limited to considering broad classes, such as excitatory and inhibitory groups[35,45,47,49].

Despite some degree of mismatch in hippocampal brain-behavioral states across clades, it is nonetheless tempting to identify possible correspondences between the present groups and identified cell classes in rodent CA1, particularly for generally conserved oscillations, such as SWRs[50,66]. We found a small number of ripple-suppressed neurons, primarily among the interneuron groups. In rodents, OLM and axo-axonic cells under anesthesia[11], and a subset of axo-axonic cells in behaving rats[67,68] decrease their firing rate during ripples, too (n.b. the OLM class activation depended on the preparation[28]). At the other extreme, the rare TORO inhibitory cells dramatically increase firing rate leading into and during ripples[69]. We had two groups showing unusually strong ripple modulations, despite overall lower firing rates, and one in particular had disproportionate ripple participation and the highest proportion of cells showing strong assembly participation; however, these tended to fire maximally at, not before, the ripple peak, unlike TORO cells. Beyond ripple modulation, PV basket cells show strong theta-locking, and strongly regulate and phase-lead pyramidal cells[70]. The cell groups we observed with strongest 4-7 Hz phase locking, however, matched pyramidal cells' phase locking and angle, and had somewhat lower overall firing rates than classic theta-locked cells. Since PV inhibitory cells are thought to play a role in memory function, mediated through hippocampal network dynamics[71–73], their recasting to fit the network dynamics of the primate brain will be an important future direction. Although the precise mapping across species is yet to be reconciled, our observations of systematic phase relationships between groups with varying frequency, offers the opportunity to identify putative groups as they arise with recent transcriptomic and synaptic-connectomic profiles in monkeys and humans, as demonstrated in rodent models[74,75].

Perhaps the most exciting finding was that CA1 pyramidal cells show different attributes by superficial/deep allocation. Similar to findings in rodents[17,22], macaque CA1 pyramidal cells in superficial and deep layers differ in average firing rate, bursting, and coefficient of variation. They showed different pairwise interactions with the inhibitory cell groups and with fine temporal specificity within several of these groups. This included deep-pyramidal cell suppression, in the context of increased superficial-cell responses, and a tightly-timed superficial-deep tradeoff among the ripple-suppressed cells, presumably arising from somatodendritic inhibitory mechanisms known to differently target pyramidal cells by depth [13,15,76,77]. Inhibitory-cell switching can determine the precisely-timed expression of independent cell types or assemblies, creating parallel channels for information transmission[78–80]. Evidence for parallel channels can be seen in their participation in cell assemblies, which are composed of either superficial or deep neurons but rarely both[22]. When added to differences in connectivity, this enables both layer-biased processing of different elements of behavioral tasks and selective coordination of extrahippocampal

activity[22]. We discovered that primate CA1 also demonstrates this cell assembly bias by strata. Because macaques also show extra-hippocampal projections that are organized by CA1 pyramidal depth[81,82], this suggests separable hippocampo-cortical networks may be organized through parallel channels within primate CA1. These findings, together with strata-specific differences in experience-dependent plasticity and in memory formation[15,21,22,83,84], suggest that their detection in primates may prove to be key to understanding how the hippocampus structures activity during memory formation.

Acknowledgments: The funding for this study was provided by National Institute of Neurological Disorders and Stroke Grant 1RF1NS127128-01, NEI (P30 EY008126), and the Whitehall Foundation Grant 100001391.

Methods:

Subjects and Behavioral Design

Two adult female macaques (*Macaca mulatta*, referred to as 'M1' and 'M2') were subjects in this study. Both monkeys underwent training in a 3D testing enclosure, which allowed them to move freely. This enclosure was equipped with multiple touchscreens distributed around its periphery. To receive a fluid reward, the monkeys needed to move sequentially to each of four touchscreens placed in one corner of the environment. On each screen, they had to touch designated objects associated with that screen, avoiding distractor objects. Their overall performance in completing the four-screen sequence determined their reward. The screens were arranged in a 2x2 array on opposite corners of the 3D space, necessitating visual search, reaching, and walking or climbing during each trial. The monkeys completed various trial blocks, which took place in both screen array corners of the testing apparatus. Following their training session, the monkeys were returned to their housing. For monkey M2, sleep recordings started immediately after the training session. For monkey M1, there were sometimes 1-2 hour gaps. Sleep epochs occurred with the monkeys in their normal housing area, with their usual social housing accommodations, in complete darkness, following the automated lighting system's overnight dark cycle. All procedures were conducted in accordance with the approved protocols and authorized procedures under the local animal care authorities (Institutional Animal Care and Use Committee).

Electrophysiological recordings

Active multichannel probes were inserted into a chronically implanted base[34], including a 128-channel probe (DA128-1, linear configuration with 40µm contact spacing) for Monkey M1 and a 64-channel probe (organized into 4 parallel shanks with 40 channels at 90 µm spacing and 3 shanks with 8 channels at 60 µm spacing) for Monkey M2 ('Deep Array' design, by Diagnostic Biochips, Inc). The probes were affixed to adjustable microdrives (M1, M2: Nano Drives, Cambridge Neurotech, Inc.; M1: custom, Rogue Research, Inc.) to facilitate precise depth positioning adjustments post-implantation, and allowing the raising and relowering (max. 7 mm or 5 mm, respectively) into target areas while remaining implanted. Post-operatively, the probes were incrementally advanced through these drives in 125mm steps until the target positions were achieved. The localization of recording sites was verified through postoperative CT scans, coregistered with pre-operative MRI data, and also by referencing functional landmarks that changed with increasing depth. Notably, the emergence of depth-specific sharp-wave ripples (SWRs) within unit-dense layers served as a key reference point. To align the 4 shanks in M2, we employed cross-correlation analysis of LFP signals observed during ripple activity across the channels. Local field potentials (LFPs) were digitally sampled at a rate of 30 kHz using the FreeLynx Wireless Acquisition system (Neuralynx, Inc) and subsequently bandpass filtered within the 0.1 Hz to 7500 Hz range. During task performance and sleep recordings for Monkey M2, data were wirelessly transmitted to the Freelynx acquisition system (Neuralynx, Inc). To optimize battery life, sleep recordings for Monkey M1 were stored on an SD card within the acquisition system. A high-frequency noise signal at approximately 6 kHz marked the point at which the battery capacity reached 10%. The onset of this noise was detected by calculating the root mean square (RMS) envelope of the band-passed filtered signal between 5800-6200 Hz. The noise initiation point was defined as the timestamp at which the RMS envelope exceeded 110% of the median value, and sleep data following this point was excluded. For the purpose of merging task and sleep recordings, data was initially converted to microvolt units, bitVolts were standardized to 0.195, and the data was subsequently transformed into binary files encoded as 16-bit integers. Sessions that exhibited no signal

loss during recording were exclusively included in the analyses. In LFP-related analyses, the raw signal was subjected to third-order Butterworth filtering with a low-pass cutoff frequency set at either 350 Hz or 450 Hz, and the data was downsampled to 1 kHz.

CT-MRI image processing and coregistration

The General Registration tool, Elastix, in the Slicer (version 4.11), was used to perform the registration of post-operative CT scans with pre-operative MRI images. The registration process maintained default parameters. Preceding registration, the CT images were cropped near to and including the cranium.

Power spectral parametrization and fitting

To estimate the layer-specific spectral content of the hippocampal and neocortical recordings, we used Welch's method with a 50%-overlapping 1024-sample sliding Hanning window to estimate power spectra for the frequency range of 1–150 Hz with a frequency resolution of 0.25 Hz. To identify spectral peaks and compare between search and rest states, we parameterized power spectra using the method described by [85]. This method models power spectra as a combination of the 1/f frequency components (aperiodic) in addition to a series of Gaussians that capture the presence of peaks (periodic components). The model was fit to a frequency range between 1 Hz and 200 Hz with a frequency resolution of 0.5 Hz. Settings for the algorithm were set as: peak width limits: (0.5, 12); max number of peaks: infinite; minimum peak height: 0; peak threshold: 2.0; and aperiodic mode: 'Fixed'.

Detecting hippocampal sharp-wave ripples

A single hippocampal LFP channel with largest ripple amplitude was selected for ripple detection. The wide-band signal was band-passed filtered between 100-180 Hz using a 3rd order Butterworth filter, and squared signal was calculated. The squared signal was further band-passed filtered in 1-20 Hz range and z-normalized. SWR peaks were detected by thresholding the normalized squared signal at 3SDs above the mean, and the surrounding SWR start and stop times were identified as crossings of 1 SDs around this peak. SWR duration limits were set to be between 20 and 400 ms. Detected events with a time interval shorter than 40 ms were merged.

Exclusion Criteria: In addition to assessing amplitude and duration, we used several criteria to identify and exclude potential false-positive ripple events.

Channel Noise Exclusion: A 'noise' channel, defined as one devoid of detectable sharp-wave ripples (SWRs) in the local field potential (LFP), was designated. Any events simultaneously detected on this channel were considered as potential false-positives, likely originating from artifacts such as electromyography.

Spectral Analysis: We conducted spectral analysis of each detected ripple event to further scrutinize its characteristics. The data was spectrally decomposed using Morlet wavelets, allowing us to compute the frequency spectrum for each event. This was achieved by averaging the normalized instantaneous amplitude within ±50 ms of the ripple peak over the frequency range of 50-200 Hz, normalized by multiplying the amplitude by the frequency. We then analyzed the number and properties of spectral peaks in each detected ripple frequency spectrum. These peaks were identified using the findpeaks function in MATLAB, considering parameters such as peak height, prominence, peak frequency, and peak width. This analysis aimed to ensure that the detected ripple events genuinely reflected high-frequency, narrowband bursts within the ripple band range. We applied multiple criteria to achieve this: first,

authentic ripple events were expected to exhibit a predominant spectral peak within the ripple band range. Therefore, if no single prominent peak (corresponding to the ripple band) was identified, the event was rejected. Additionally, authentic ripple events were anticipated to display a limited narrowband burst; thus, if the ripple-peak had an excessively wide peak width (indicating more broadband spectral changes) or prominent high-frequency activity, the event was considered for rejection (see[86]).

Visual Inspection: Finally, all detected ripples underwent visual inspection, and any events flagged as false-positives during this process were subsequently removed from the dataset.

Spike sorting

Spike sorting was performed using Kilosort 1.0 ([87], https://github.com/cortex-lab/KiloSort). The process involved applying a 300-Hz high-pass filter to the raw signals, followed by whitening the data in blocks of 32 channels. Parameters relevant to automated sorting are detailed in the table.

Removing putative double-counted spikes[88]***.*** The Kilosort algorithm will occasionally fit a template to the residual left behind after another template has been subtracted from the original data, resulting in double-counted spikes. Such double-counted spikes could artificially inflate inter-spike interval (ISI) violations for a single unit or create erroneous zero-time-lag synchrony between neighboring units. Consequently, spikes with peak times within a 5e-4 second interval and peak waveforms detected on the same channels were systematically removed from the dataset.

*Removing units with artefactual waveforms****.*** Kilosort1 generates templates of a fixed length (2 ms) that matches the time course of an extracellularly detected spike waveform. However, there are no constraints on template shape, which means that the algorithm often fits templates to voltage fluctuations with characteristics that could not physically result from the current flow associated with an action potential. The units associated with these templates are considered 'noise' and are removed on the basis of spread (waveform appears on many channels), and shape (e.g. no peak and trough or sinusoidal waveform) criteria and autocorrelogram function.

Manual curation and re-clustering with Phy. Manual curation and re-clustering were performed using Phy (https://github.com/kwikteam/phy). Kilosort-derived clusters were imported into Phy for manual curation. Units that were poorly isolated according to the initial Kilosort results were re-clustered using Klusta with custom-designed plugins (https://github.com/petersenpeter/phyplugins) to obtain well-isolated single units. The quality of these clusters was evaluated based on refractory period violations and Fisher's linear discriminant metrics. Noise clusters and poorly isolated units were subsequently excluded from the analysis.

Kilosort Parameters

ops.datatype	'dat'
ops.fs	30000
ops.Nfilt	1024
ops.whitening	'full'
ops.nSkipCov	1
ops.whiteningRange	32
ops.criterionNoiseChannels	0.2
ops.Nrank	3

ops.nfullpasses	6
ops.maxFR	20000
ops.fshigh	300
ops.ntbuff	64
ops.scaleproc	200
ops.NT	32*1024+ ops.ntbuff
ops.Th	[4 10 10]
ops.lam	[10 30 30]
ops.nannealpasses	4
ops.momentum	1./[20 400]
ops.shuffle_clusters	1
ops.mergeT	0.1
ops.splitT	0.1
ops.initialize	'fromData'
ops.spkTh	-4
ops.loc_range	[3 1]
ops.long_range	[30 6]
ops.maskMaxChannels	5
ops.crit	0.65
ops.nFiltMax	10000

Localization of neuronal somata within the CA1 layers

To estimate the location of the linear-array channels relative to CA1 layers, we used features of the sharp wave ripple. The sharp wave component of the SWR arises from CA3 Schaffer collateral inputs that generate a current sink in stratum radiatum (SR) with a return source centered in stratum pyramidale[89]. In the relatively closed fields of rat or mouse CA1, this is evident as a polarity reversal between SR and the deeper layers, where the envelope flattens, distorts and ultimately reverses[6]. The source/sink gradient has been used as a depth reference to identify superficial/deep pyramidal cells[22], and should be more sensitive to local generators (more tolerant of open-fields) than the raw fields[90–92]. On this basis, we first estimated the radiatum/pyramidale transition using current source density (CSD), the second spatial derivative, of ripple-trigger averaged signal across the regularly-spaced LFP channels. This identified the general regions of SR and SP. Next, we calculated ripple power and the slope of sharp-wave envelope peak, both of which have been used to center the pyramidal layer in previous studies[17,22], respectively. For each session, we set the channel closest to the LFP slope zero-crossing as 0, and the depth of the other channels in relation to that point, considering the fixed inter-electrode distance. No additional scaling was made to the inter-channel distances. This reversal point fell in the middle of sinks and sources of CSD and above the depth of maximum ripple power. For the side-shank linear sites (in M2), we adjusted the physiological depth based on the correlational similarity of mean sharp-wave ripple LFP. For all isolated units, the site with the largest spike amplitude for each unit was regarded as the location of the cell body.

Cell type classification

To establish the feature space for cell type classification, we leveraged single-unit waveforms and interspike interval (ISI) distributions of the cells. The filtered single-unit waveforms (comprising 48 samples

at 30 kHz) were first normalized within the range of 0 to 1 and aligned. Subsequently, we used the Uniform Manifold Approximation and Projection (UMAP) to reduce the dimensionality of the waveform matrix to 2 components. In a parallel process, the log10 ISI distributions within the range of 0-10 seconds were subjected to UMAP analysis to obtain 2 components as well. For these UMAP procedures, we employed a custom UMAP function implemented in MATLAB[93]. The selection of UMAP parameters was guided by consultation with[51]. To generate the feature space for clustering, the four attributes (two from waveform and two from ISI) were concatenated. Clustering was performed using Spectral Clustering in MATLAB, with Mahalanobis distance serving as the primary metric. Initially, we set the number of clusters to 20, based on the criteria of AIC and BIC applied to Gaussian mixture models (GMM) built on the feature space. Subsequent refinements were carried out on the initial clusters using either spectral or GMM clustering techniques, with similar clusters being merged.

UMAP Parameters:

min_dist	0.1
n_neighbors	20
n_components	2
n_epochs	5000
metric	euclidean

Classification of deep and superficial CA1 pyramidal cells

The first group was designated the pyramidal cell group, because these cells demonstrated the low firing rates, high propensity for bursting, and dense localization within the Stratum Pyramidale that are the hallmarks of CA1 pyramidal cells[46,53,54]. For the superficial and deep analyses, we removed from this group the spatial outliers (with relative depths falling outside the 5-95th depth percentile range), and cells with mean firing rates > 1 Hz or a burst index exceeding 3, before calculating the median depth of these units to segregate into superficial and deep categories. The spatial distribution of CA1sup neurons spanned from -300 to 540 µm, and for CA1deep neurons, it extended from -630 to -330 µm.

Burst Index

We calculated a burst index to capture the propensity of neurons to discharge in bursts (i.e. short intervals, or “complex spikes”). This was estimated from the mean of spike auto-correlogram (1 ms bin size) measured between 1 and 10 ms, normalized by the mean value between 200 and 300 ms[76,94].

Ripple-associated spike content analysis

Within-SWR firing rate was calculated as the number of spikes during SWRs divided by the cumulative duration of the SWRs between the first and last spike fired by the cell. The ripple participation probability of individual units was defined as the fraction of SWRs in which that neuron fired at least one spike. Ripple ratio was defined as firing rate during ripple events divided by the overall firing rate.

To calculate spike density functions, spike vectors of individual cells were binned with 1 ms binsize and peri-event time histograms (PETHs) were computed locked to ripple peaks and converted to rate. Then a gaussian kernel with a 10 ms S.D. was applied to the PETHs to obtain spike densities. For each cell, we calculated the baseline activity as the mean firing rate of a shuffled surrogate dataset created for that cell and subtracted this value from the original PETH.

To test the hypothesis that spiking activity of single cells are modulated surrounding the ripple peak, we derived nonripple event surrogates. These surrogates were created for individual cells using timestamps selected randomly without replacement from recording epochs when ripples were not detected. We matched the number of ripple and nonripple surrogate events (n observed ripple events = n nonripple events). Furthermore, to ensure that signal properties were maximally matched between target events and surrogates, surrogates were drawn only from a 10-min time window before and after the corresponding ripple event. To test the significant difference between the ripple-locked and surrogate spike densities, we used a cluster-based permutation procedure using 5000 permutations and a cluster threshold of $p < 0.05$ and a final threshold for significance of $p < 0.05$.

Spike-field synchronization

To quantify spike-field synchronization, we used the pairwise phase consistency (PPC) measure, which is unbiased by the number of spikes[95]. For hippocampal recordings, we selected the sharp-wave ripple channel in the Stratum Pyramidal of the CA1 across sessions. If the unit spikes were from this channel, we used an adjacent channel to measure the PPC. The spectral content was estimated with Morlet wavelet decomposition method using a constant number of cycles (7) per frequency for frequencies between 1 and 200 Hz with a frequency resolution of 1 Hz. We measured PPC values separately for spikes during wakeful and rest/sleep states, and only for neurons that fired at least 100 spikes[95]. One caveat of this approach is that it assumes signals to be oscillatory and, additionally, sinusoidal. This can distort preferred phase estimations. We used an alternative approach to estimate phase of modulation in restricted time windows of presumed oscillatory bouts, across frequency ranges. For each frequency group, LFP signal was filtered in the specified frequency band using a 3rd Butterworth filter. Next, instantaneous phase and power were derived from Hilbert transform. A phase value was assigned to each action potential during significant periods (power of filtered LFP > 2 S.D. above the mean) using linear interpolation. Peaks are at 0° and 360° and troughs at 180° throughout the paper. Then we calculated the mean phase and resultant vector using the circular statistics toolbox on MATLAB[96] (https://github.com/circstat/circstat-matlab). To find the grand mean phase and resultant vector of a cell group in a specific frequency, we measured the mean phase of firing for included members of that cell group and then calculated the mean phase and resultant vector of the mean phases. The grand mean phase and resultant vector determines the consistency of phase of firing among the members of a cell group. For the calculation of the grand mean phase, we included only cells that had at least 20 spikes during significant epochs of interest. We set a significance threshold of $p = 0.01$ using the Rayleigh test for phase locking.

Pairwise cell interaction

We used two complementary approaches to estimate pairwise cell interactions. First, recordings were segmented into 25 ms time bins, and for each neuron, the number of spikes within each bin was counted and converted to firing rate. Subsequently, we convolved the spike vectors with a Gaussian kernel, with a standard deviation calculated as binsize / (2 * sqrt(2 * log(2))) (converted to Full Width at Half Maximum, FWHM). Pearson's correlation coefficients were calculated between the spike density vectors of different neurons, serving as a measure of their co-firing tendencies.

To prevent global periods of inactivity or instability from influencing the Pearson's coefficients, we only considered correlations if two conditions were met: 1) the overlapping windows of activity exceeded 5 minutes, and 2) both cells fired at least 100 spikes within the overlapping time window.

Additionally, cross-correlograms (CCGs) were computed between pairs of neurons with a 1 ms bin resolution and converted to rate (CCG divided by the reference cell's number of spikes per time bin). These CCGs were smoothed using a zero-lag partially hollowed Gaussian filter with a convolving window of 5 ms and a hollow fraction of 0.6 [77,97].

The mean activity in a baseline window (-50 to -20 ms) was subtracted from the original CCGs to selectively evaluate the fine temporal interactions (+/- 20 ms). To assess the statistical significance of CCGs, we created surrogate spike time series' by shuffling the inter-spike intervals of the cells [98] and calculating their CCGs. This process was repeated 5000 times to generate a surrogate distribution of CCGs. P-values were computed for each time bin of the CCG (-20 to 20 ms) and subjected to multiple-comparison correction using the Benjamini and Hochberg False Discovery Rate (FDR) procedure To compare CCGs between the CA1sup and CA1deep groups, a two-sample permutation test (n=5000) with Tmax correction was used [99].

Assembly pattern identification and activation strength

Cell assemblies were identified during sleep recordings as previously described[22,100–104]. Significant co-firing patterns were detected using an unsupervised statistical method based on independent component analysis (ICA). The spike trains for each neuron were binned into time windows of 90 ms (corresponding to the 90th percentile of ripple durations) and z-score transformed to eliminate biases due to differences in average firing rates. This creates for each session, a cell x binned firing rate matrix (Z). Next, a principal component analysis was applied to the matrix (Z). For this, the correlation matrix of Z was given by $C = \frac{1}{n}ZZ^T$ and the eigenvalue decomposition of C was given by:

$$\sum_{j=1}^{n} \lambda_j p_j p_j^T = \frac{1}{n} ZZ^T$$

where λ_j is the jth eigenvalue of C and p_j is its corresponding eigenvector. The Marcenko-Pastur law was used to estimate the number of significant patterns embedded within Z. For a nXB matrix, an eigenvalue exceeding λ_{max}, defined by $\lambda_{max} = (1 + \sqrt{n/B})^2$, signifies that the pattern given by the corresponding principal component explains more correlation than would be expected if the neurons were independent of each other. The number of eigenvalues exceeding λ_{max} was defined as NA and therefore represents the minimum number of distinct significant patterns in the data. The significant principal components were then projected back onto the binned spike data

$$Z_{PROJ} = P_{SIGN}^T Z$$

where P_{SIGN} is the nXNA matrix with the NA principal components as columns.

Independent component analysis (ICA), using the fast ICA algorithm (http://research.ics.aalto.fi/ica/fastica), was then applied to the matrix ZPROJ. That is, an NAXNA unmixing matrix W was found such that the rows of the matrix $Y = W^T Z_{PROJ}$ were as independent as possible. The arbitrary signs of the independent component (IC) weights were set so that the highest absolute weight was positive. The unmixing matrix W was then used to derive each cell's weight within each assembly $V = P_{SIGN} W$ where the columns of V $(i.e., v_1, \dots, v_{NA})$ are the weight vectors of the assembly patterns.

To determine the strength of the expressed assemblies, we tracked each assembly pattern v_k over time by:

$$R_k(t) = z(t)^T P_k z(t)$$

where $z(t)$ is a smooth vector function containing for each neuron its z-scored instantaneous firing rate and P_k is the matrix projecting $z(t)$ to the activation strength of the assembly pattern k at time t.

Organization of cell assemblies

The majority of the identified assembly patterns had a characteristic distribution whereby a few neurons displayed high weights, while a larger group of neurons had weights approximating zero. To determine the significant membership corresponding to each assembly pattern, we used the criterion that the member neurons of an assembly should have weights exceeding the mean weight by at least two standard deviations. All subsequent analyses were conducted directly on the assembly patterns themselves, using the weight vectors derived from the contribution of all recorded neurons. Based on the composition of significant assembly members, the assemblies were classified into three distinct groups. **Within Assemblies:** These assemblies had at least one significant member from the pyramidal cell group. If all significant pyramidal members were exclusively from the superficial or deep regions, we labeled the assembly as "within superficial" or "within deep," respectively. **Across Assemblies:** These assemblies included at least one significant member from each of the superficial and deep pyramidal cell groups. **Non-pyramidal cell assemblies:** This category included assemblies that didn't have any significant pyramidal cell members.

To estimate the probability of realization of a specific assembly organization, we used the binomial probability density function (binopdf in MATLAB). Observed and expected probabilities were computed as:

$$ObservedProb = binopdf(sigDeep, sigSup + sigDeep, NDeep/(NSup + NDeep));$$

$$PallDeep = binopdf(sigSup + sigDeep, sigSup + sigDeep, NDeep/(NSup + NDeep));$$

$$PallSup = binopdf(sigSup + sigDeep, sigSup + sigDeep, NSup/(NSup + NDeep));$$

$$ExpectedProb = 1 - (PallSup + PallDeep);$$

Where $sigDeep$ and $sigSup$ represent the number of significant CA1deep and CA1sup members within the assembly, respectively. $NDeep$ and $NSup$ denote the total number of recorded CA1deep and CA1sup neurons within the session. $ObservedProb$ signifies the probability of encountering the specific organization of the assembly. $PallDeep$ and $PallSup$ indicate the probability that all significant pyramidal members exclusively belong to either CA1deep or CA1sup. $ExpectedProb$ reflects the anticipated probability that the assembly could belong to the "across" category.

Assembly participation probability was calculated for all cells per session and it was defined as the number of assemblies where a cell participated as a significant member divided by the total number of detected assemblies in a session.

Statistical analysis

Data collection was conducted prior to (thus blind to) the clustered cell groups. The sharp wave ripple and general spiking activity were the main features determining any change made to electrode depth. Data analysis and behavioral experiments did not require manual scoring. No specific methodology was used to estimate the minimum required population sample, due to no knowledge of the (cell group, assembly) population sizes during data collection; however, the number of animals and sessions and the general registration of unit activity across channels was comparable to or greater than those used in prior studies. All statistical analyses were performed using MATLAB R2021a, utilizing non-parametric methods for comparisons of means and variances, including Kruskal-Wallis analysis of variance, two-sample permutation tests, one-sample randomization tests.

Two-sample permutation test: A two-sample permutation test is a statistical method used to compare two independent groups or samples in a hypothesis testing framework. It is particularly valuable when the data do not meet the assumptions of parametric tests like the t-test. For comparison in which each sample had a single data point, we shuffled the membership assignments, computed the mean difference between the surrogate samples, and repeated this process 5000 times to create a surrogate probability distribution of mean differences. The original, non-permuted data are then compared to the surrogate distribution to obtain uncorrected p-values.

For *cluster-based multiple comparison correction*, all samples with p-values smaller than 0.05 were selected. These selected samples were subsequently clustered into connected sets based on their adjacency, and the size of each cluster was calculated. This process was repeated 5000 times to generate a distribution of cluster sizes. Clusters with sizes exceeding the cluster threshold at the 95th quantile were reported as significant [105].

For CCG analyses we controlled family-wise error rate (FWER) using the Tmax correction method [99]. This method provides strong control of FWER, even for small sample sizes, and is much more powerful than traditional correction methods [106,107]. It is also relativelyinsensitive to differences in population variance when samples of equal size are used [108].

One-Sample Randomization Test: This test, akin to the permutation test, involved comparing a time series against a surrogate dataset created from randomly selected timestamps.

For all other posthoc tests, either Tukey-Kramer or the Benjamini & Hochberg multiple comparison correction was applied, as specified in the main text.

Boxplots were used to present data, with the median, 25th, and 75th percentiles represented within the box, and the whiskers illustrating the data range. In cases where boxplots did not display individual data points, outliers were excluded from the plots but were consistently included in the statistical analysis.

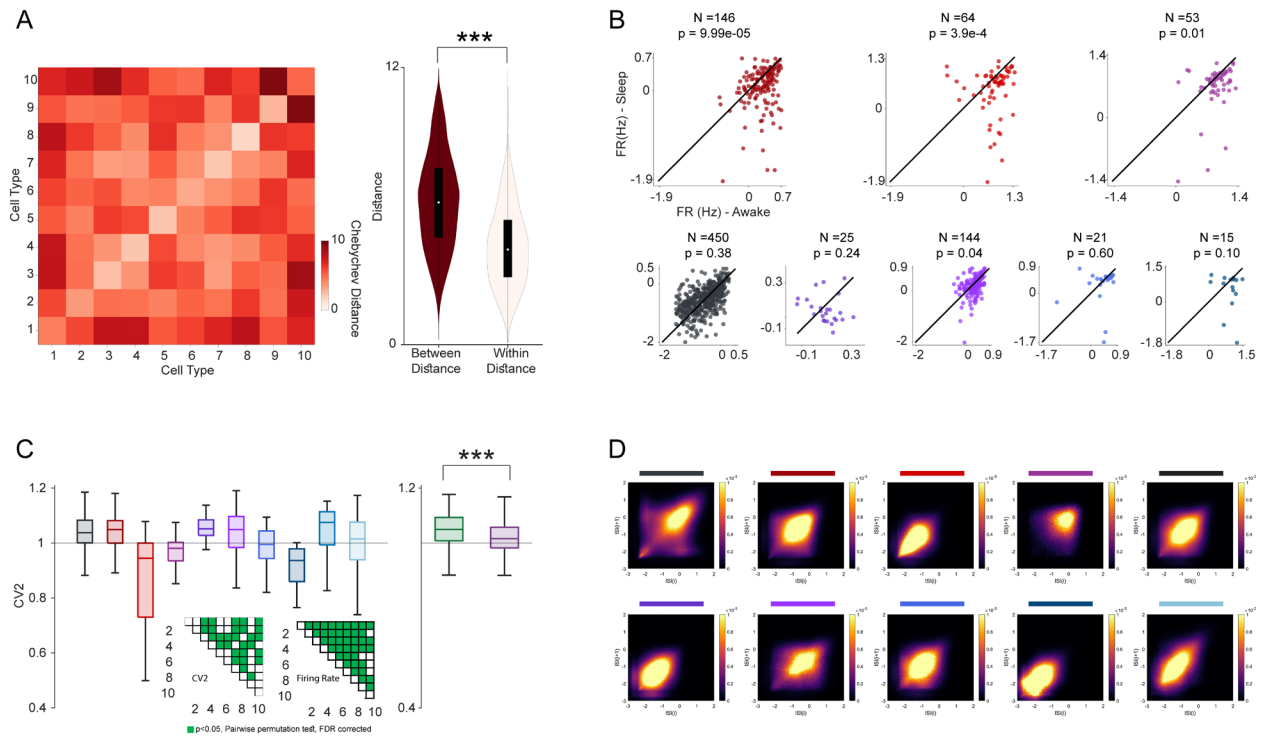

Figure S1: Physiological features of cell groups in CA1 (A) Left: Chebyshev distance matrix in feature space, for cells according to assigned cell group. Note that the diagonal values are smaller than off-diagonal, indicating that within-group members were closer together in the feature space compared to between-group members. Right: Distribution of between-group (red), and within-group (bone white) of distance values ($p < 0.001$, two-sample permutation test) **(B)** Comparison of cells' firing rates during sleep compared to wakeful states, organized by cell group. The color of the data points indicated the cell group evaluated per plot. (N = number of cells; p = result of a two-sample permutation test). **(C)** Left: Distribution of ISI-based coefficients of variance (CV2) for each cell group. Right: CV2 for superficial versus deep pyramidal cell groups ($p<0.001$, two-sample permutation test). Inset: the left matrix shows the result of pairwise permutation tests following significant Kruskal-Wallis test, $p < 0.001$; dark pixels indicate $p < 0.05$). The right matrix shows the same for firing rate. **(D)** Joint ISI histograms showing the next interval (ISI_{i+1}) as a function of the current interval (ISI_i) for eight cell groups. Horizontal bars indicate cell group.

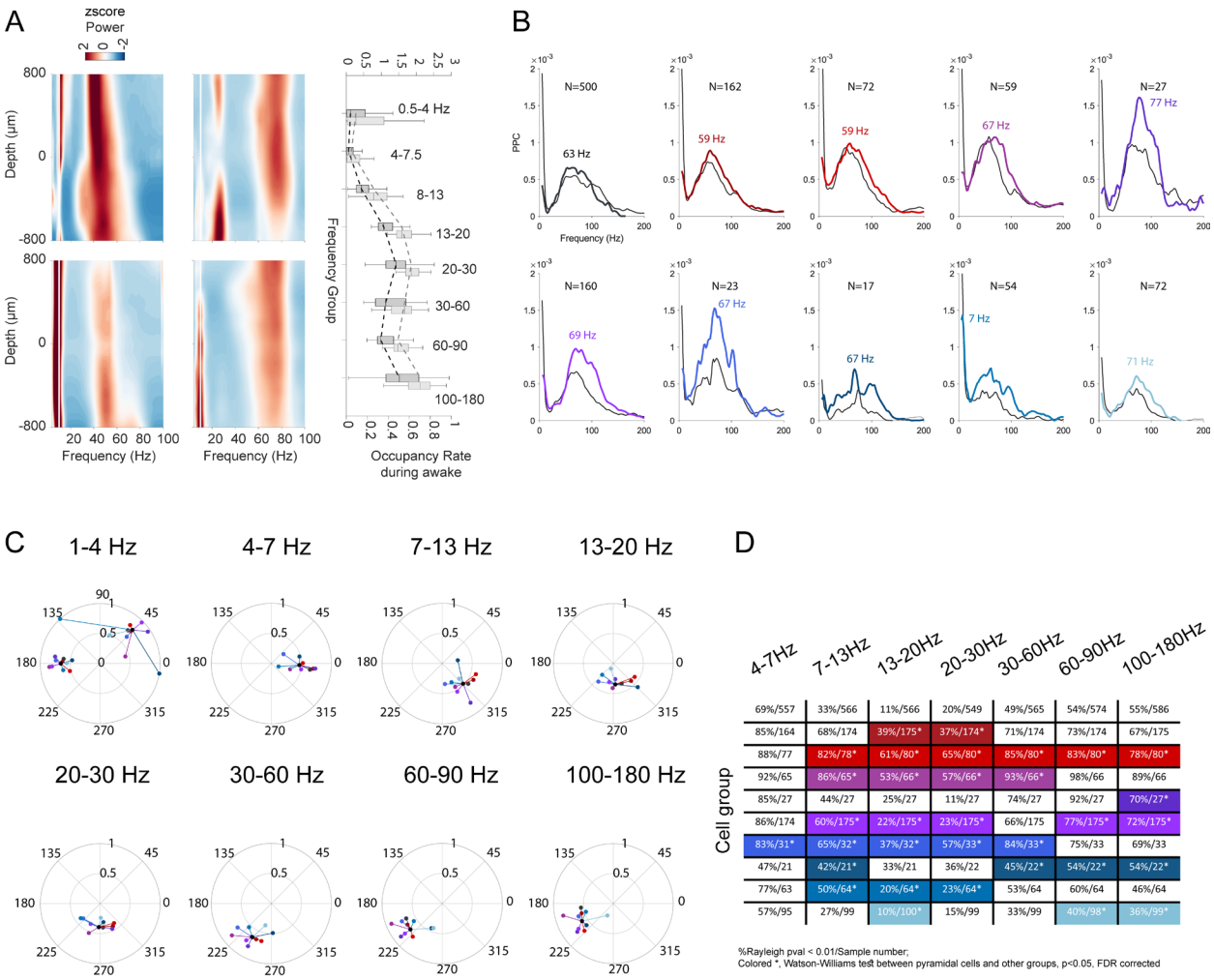

D

Cell group	4-7Hz	7-13Hz	13-20Hz	20-30Hz	30-60Hz	60-90Hz	100-180Hz
	69%/557	33%/566	11%/566	20%/549	49%/565	54%/574	55%/586
	85%/164	68%/174	39%/175*	37%/174*	71%/174	73%/174	67%/175
	88%/77	82%/78*	61%/80*	65%/80*	85%/80*	83%/80*	78%/80*
	92%/65	86%/65*	53%/66*	57%/66*	93%/66*	98%/66	89%/66
	85%/27	44%/27	25%/27	11%/27	74%/27	92%/27	70%/27*
	86%/174	60%/175*	22%/175*	23%/175*	66%/175	77%/175*	72%/175*
	83%/31*	65%/32*	37%/32*	57%/33*	84%/33*	75%/33	69%/33
	47%/21	42%/21*	33%/21	36%/22	45%/22*	54%/22*	54%/22*
	77%/63	50%/64*	20%/64*	23%/64*	53%/64	60%/64	46%/64
	57%/95	27%/99	10%/100*	15%/99	33%/99	40%/98*	36%/99*

%Rayleigh pval < 0.01/Sample number;
Colored *, Watson-Williams test between pyramidal cells and other groups, p<0.05, FDR corrected

Figure S2: Spectral profiles and spike-field relationships (A) Left: 1/f corrected FOOOF power spectrum across depths of recording in CA1 during task (top) and rest/sleep (bottom) for each animal (M1, left; z-normalized per channel). Right: Corrected (black, top axis) and balanced (grey, bottom axis) proportion of detected oscillatory bouts during task versus sleep states across frequency bands. LFP channels were selected from Stratum Radiatum. **(B)** Mean PPC values during task (colored) and rest/sleep (grey). The peak frequencies during task are listed. **(C)** Spike phase-of-firing plots separated for each frequency band. Each plot shows, for the specified frequency band, the grand mean phase (black) and distance to each cell group's resultant vector, taken from distribution of the underlying cells' resultant vectors. Note that for the 1-4 Hz group, we separated the results for the 2 animal subjects due to conspicuous differences between them, unique to this plot. **(D)** The matrix shows the results of pairwise permutation tests between the pyramidal cell group and other groups, for each frequency band ($p < 0.05$, two-sample Watson-Williams test, FDR corrected)

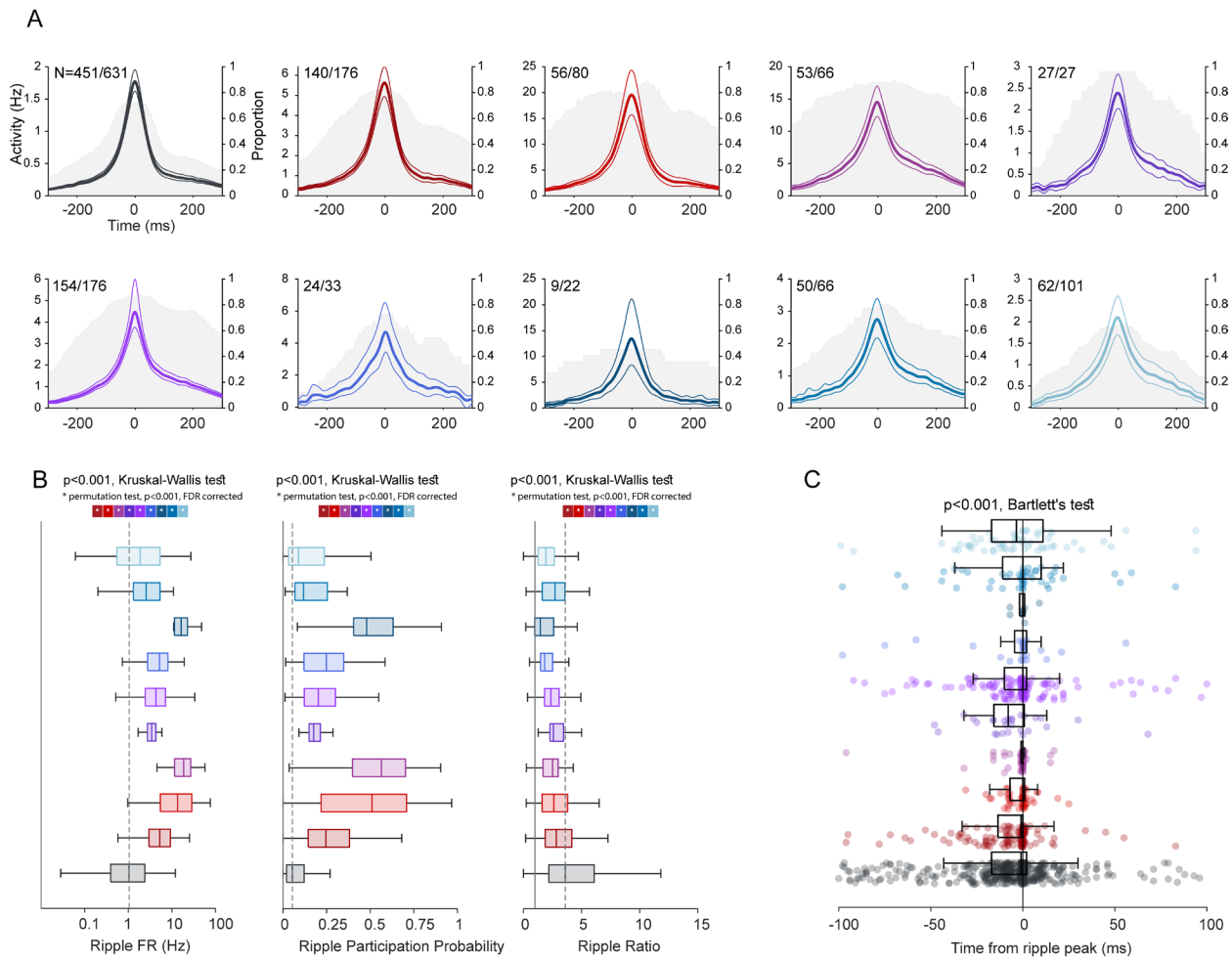

Figure S3: Sharp-wave ripple-associated spiking dynamics (A) Ripple-aligned spike density (mean + 95% CI) for significantly modulated cells of different groups. N: Significantly modulated/total cells in the group. Proportion of significantly modulated units are shown in the shaded area plots, with proportions listed on the right axis ($p < 0.05$, one-sample cluster-based permutation test). **(B)** Left: Ripple firing rate across cell groups; dotted line indicates PYR group median. Middle: Ripple participation probability. Right: Ripple ratio (average firing rate during ripples / overall firing rate) by cell group, with ratio = 1 indicated by black line. Dotted line indicates PYR group. All plots show ($p < 0.001$, Kruskal-Wallis test) and asterisks in color coded box show the result of post-hoc pairwise permutation tests between the pyramidal cell group and all other cell groups (* $p < 0.001$, FDR corrected). **(C)** The distribution of peak response times around the ripple peak, separated by cell group. ($p < 0.001$, Bartlett's test for equality of variances).

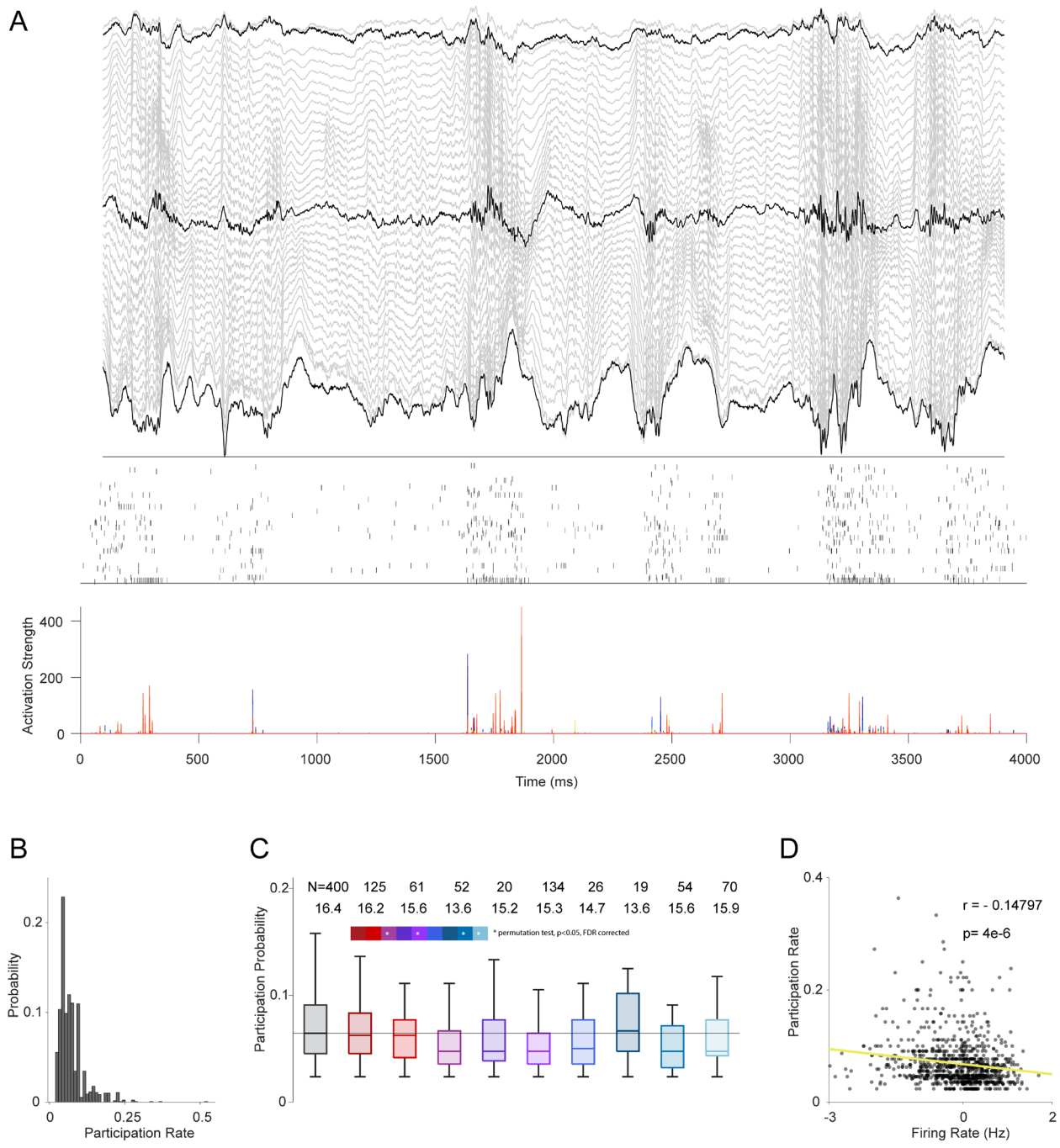

Figure S4: Organization of assembly dynamics (A) Top: Example LFP traces across depth of recording in CA1 during sleep. Middle: Raster plot of simultaneously recorded units. Bottom: Assembly activation strength. Each assembly is assigned a different color. **(B)** Distribution of assembly participation rate for each cell group. Cells with a participation rate of 0 were removed from the analysis. **(C)** Distribution of assembly participation probability for each cell group ($p < 0.001$, Kruskal-Wallis test). The first row of numbers shows number of recorded units that participated in at least one assembly. The second row of numbers reports the average number of assemblies available to participate in, for each cell group, across session. The thin black line indicates the pyramidal cell median. The color-vector shows the post-hoc pairwise permutation test between pyramidal cell group with all other cell groups. (* p <

0.05, FDR corrected) **(D)** Relationship between firing rate of neurons and assembly participation rate, revealing an inverse correlation (r = -0.14, p < 0.001 t-test).

1. Eichenbaum, H., Dudchenko, P., Wood, E., Shapiro, M., and Tanila, H. (1999). The hippocampus, memory, and place cells: is it spatial memory or a memory space? Neuron *23*, 209–226. 10.1016/s0896-6273(00)80773-4.

2. Colgin, L.L. (2016). Rhythms of the hippocampal network. Nat. Rev. Neurosci. *17*, 239–249. 10.1038/nrn.2016.21.

3. Hasselmo, M.E. (2005). What is the function of hippocampal theta rhythm?--Linking behavioral data to phasic properties of field potential and unit recording data. Hippocampus *15*, 936–949. 10.1002/hipo.20116.

4. Oliva, A., Fernandez-Ruiz, A., and Karaba, L.A. (2023). CA2 orchestrates hippocampal network dynamics. Hippocampus *33*, 241–251. 10.1002/hipo.23495.

5. He, H., Wang, Y., and McHugh, T.J. (2023). Behavioral status modulates CA2 influence on hippocampal network dynamics. Hippocampus *33*, 252–265. 10.1002/hipo.23498.

6. Buzsáki, G., Leung, L.W., and Vanderwolf, C.H. (1983). Cellular bases of hippocampal EEG in the behaving rat. Brain Res. *287*, 139–171. 10.1016/0165-0173(83)90037-1.

7. Buzsáki, G., and Moser, E.I. (2013). Memory, navigation and theta rhythm in the hippocampal-entorhinal system. Nat. Neurosci. *16*, 130–138. 10.1038/nn.3304.

8. Harris, K.D., Hochgerner, H., Skene, N.G., Magno, L., Katona, L., Bengtsson Gonzales, C., Somogyi, P., Kessaris, N., Linnarsson, S., and Hjerling-Leffler, J. (2018). Classes and continua of hippocampal CA1 inhibitory neurons revealed by single-cell transcriptomics. PLoS Biol. *16*, e2006387. 10.1371/journal.pbio.2006387.

9. Franjic, D., Skarica, M., Ma, S., Arellano, J.I., Tebbenkamp, A.T.N., Choi, J., Xu, C., Li, Q., Morozov, Y.M., Andrijevic, D., et al. (2022). Transcriptomic taxonomy and neurogenic trajectories of adult human, macaque, and pig hippocampal and entorhinal cells. Neuron *110*, 452-469.e14. 10.1016/j.neuron.2021.10.036.

10. Freund, T.F., and Buzsáki, G. (1996). Interneurons of the hippocampus. Hippocampus *6*, 347–470. 10.1002/(SICI)1098-1063(1996)6:4<347::AID-HIPO1>3.0.CO;2-I.

11. Klausberger, T., Magill, P.J., Márton, L.F., Roberts, J.D.B., Cobden, P.M., Buzsáki, G., and Somogyi, P. (2003). Brain-state- and cell-type-specific firing of hippocampal interneurons in vivo. Nature *421*, 844–848. 10.1038/nature01374.

12. Slomianka, L., Amrein, I., Knuesel, I., Sørensen, J.C., and Wolfer, D.P. (2011). Hippocampal pyramidal cells: the reemergence of cortical lamination. Brain Struct. Funct. *216*, 301–317. 10.1007/s00429-011-0322-0.

713 13. Lee, S.-H., Marchionni, I., Bezaire, M., Varga, C., Danielson, N., Lovett-Barron, M., Losonczy, A.,
714 and Soltesz, I. (2014). Parvalbumin-positive basket cells differentiate among hippocampal
715 pyramidal cells. Neuron *82*, 1129–1144. 10.1016/j.neuron.2014.03.034.

716 14. Masurkar, A.V., Srinivas, K.V., Brann, D.H., Warren, R., Lowes, D.C., and Siegelbaum, S.A. (2017).
717 Medial and Lateral Entorhinal Cortex Differentially Excite Deep versus Superficial CA1 Pyramidal
718 Neurons. Cell Rep. *18*, 148–160. 10.1016/j.celrep.2016.12.012.

719 15. Valero, M., Cid, E., Averkin, R.G., Aguilar, J., Sanchez-Aguilera, A., Viney, T.J., Gomez-Dominguez,
720 D., Bellistri, E., and de la Prida, L.M. (2015). Determinants of different deep and superficial CA1
721 pyramidal cell dynamics during sharp-wave ripples. Nat. Neurosci. *18*, 1281–1290.
722 10.1038/nn.4074.

723 16. Kohara, K., Pignatelli, M., Rivest, A.J., Jung, H.-Y., Kitamura, T., Suh, J., Frank, D., Kajikawa, K.,
724 Mise, N., Obata, Y., et al. (2014). Cell type-specific genetic and optogenetic tools reveal
725 hippocampal CA2 circuits. Nat. Neurosci. *17*, 269–279. 10.1038/nn.3614.

726 17. Mizuseki, K., Diba, K., Pastalkova, E., and Buzsáki, G. (2011). Hippocampal CA1 pyramidal cells
727 form functionally distinct sublayers. Nat. Neurosci. *14*, 1174–1181. 10.1038/nn.2894.

728 18. Geiller, T., Fattahi, M., Choi, J.-S., and Royer, S. (2017). Place cells are more strongly tied to
729 landmarks in deep than in superficial CA1. Nat. Commun. *8*, 14531. 10.1038/ncomms14531.

730 19. Sharif, F., Tayebi, B., Buzsáki, G., Royer, S., and Fernandez-Ruiz, A. (2021). Subcircuits of Deep and
731 Superficial CA1 Place Cells Support Efficient Spatial Coding across Heterogeneous Environments.
732 Neuron *109*, 363-376.e6. 10.1016/j.neuron.2020.10.034.

733 20. Danielson, N.B., Zaremba, J.D., Kaifosh, P., Bowler, J., Ladow, M., and Losonczy, A. (2016).
734 Sublayer-Specific Coding Dynamics during Spatial Navigation and Learning in Hippocampal Area
735 CA1. Neuron *91*, 652–665. 10.1016/j.neuron.2016.06.020.

736 21. Gu, L., Ren, M., Lin, L., and Xu, J. (2023). Calbindin-expressing CA1 pyramidal neurons encode
737 spatial information more efficiently. eNeuro. 10.1523/ENEURO.0411-22.2023.

738 22. Harvey, R.E., Robinson, H.L., Liu, C., Oliva, A., and Fernandez-Ruiz, A. (2023). Hippocampo-cortical
739 circuits for selective memory encoding, routing, and replay. Neuron *111*, 2076-2090.e9.
740 10.1016/j.neuron.2023.04.015.

741 23. Berndt, M., Trusel, M., Roberts, T.F., Volk, L.J., and Pfeiffer, B.E. (2022). Bidirectional synaptic
742 changes in deep and superficial hippocampal neurons following *in vivo* activity. BioRxiv.
743 10.1101/2022.10.27.514077.

744 24. Klausberger, T., and Somogyi, P. (2008). Neuronal diversity and temporal dynamics: the unity of
745 hippocampal circuit operations. Science *321*, 53–57. 10.1126/science.1149381.

746 25. Pelkey, K.A., Chittajallu, R., Craig, M.T., Tricoire, L., Wester, J.C., and McBain, C.J. (2017).
747 Hippocampal gabaergic inhibitory interneurons. Physiol. Rev. *97*, 1619–1747.
748 10.1152/physrev.00007.2017.

26. Klausberger, T., Marton, L.F., O'Neill, J., Huck, J.H.J., Dalezios, Y., Fuentealba, P., Suen, W.Y., Papp, E., Kaneko, T., Watanabe, M., et al. (2005). Complementary roles of cholecystokinin- and parvalbumin-expressing GABAergic neurons in hippocampal network oscillations. J. Neurosci. *25*, 9782–9793. 10.1523/JNEUROSCI.3269-05.2005.

27. Lasztóczi, B., and Klausberger, T. (2014). Layer-specific GABAergic control of distinct gamma oscillations in the CA1 hippocampus. Neuron *81*, 1126–1139. 10.1016/j.neuron.2014.01.021.

28. Varga, C., Golshani, P., and Soltesz, I. (2012). Frequency-invariant temporal ordering of interneuronal discharges during hippocampal oscillations in awake mice. Proc Natl Acad Sci USA *109*, E2726-34. 10.1073/pnas.1210929109.

29. Dudok, B., Klein, P.M., Hwaun, E., Lee, B.R., Yao, Z., Fong, O., Bowler, J.C., Terada, S., Sparks, F.T., Szabo, G.G., et al. (2021). Alternating sources of perisomatic inhibition during behavior. Neuron *109*, 997-1012.e9. 10.1016/j.neuron.2021.01.003.

30. Forro, T., and Klausberger, T. (2023). Differential behavior-related activity of distinct hippocampal interneuron types during odor-associated spatial navigation. Neuron *111*, 2399-2413.e5. 10.1016/j.neuron.2023.05.007.

31. Dupret, D., O'Neill, J., and Csicsvari, J. (2013). Dynamic reconfiguration of hippocampal interneuron circuits during spatial learning. Neuron *78*, 166–180. 10.1016/j.neuron.2013.01.033.

32. McKenzie, S. (2018). Inhibition shapes the organization of hippocampal representations. Hippocampus *28*, 659–671. 10.1002/hipo.22803.

33. Abbaspoor, S., Hussin, A.T., and Hoffman, K.L. (2023). Theta- and gamma-band oscillatory uncoupling in the macaque hippocampus. eLife *12*. 10.7554/eLife.86548.

34. Talakoub, O., Sayegh, P.F., Womelsdorf, T., Zinke, W., Fries, P., Lewis, C.M., and Hoffman, K.L. (2019). Hippocampal and neocortical oscillations are tuned to behavioral state in freely-behaving macaques. BioRxiv. 10.1101/552877.

35. Leonard, T.K., Mikkila, J.M., Eskandar, E.N., Gerrard, J.L., Kaping, D., Patel, S.R., Womelsdorf, T., and Hoffman, K.L. (2015). Sharp Wave Ripples during Visual Exploration in the Primate Hippocampus. J. Neurosci. *35*, 14771–14782. 10.1523/JNEUROSCI.0864-15.2015.

36. Green, J.D., and Arduini, A.A. (1954). Hippocampal electrical activity in arousal. J. Neurophysiol. *17*, 533–557. 10.1152/jn.1954.17.6.533.

37. Tamura, R., Nishida, H., Eifuku, S., Fushiki, H., Watanabe, Y., and Uchiyama, K. (2013). Sleep-stage correlates of hippocampal electroencephalogram in primates. PLoS ONE *8*, e82994. 10.1371/journal.pone.0082994.

38. Bódizs, R., Kántor, S., Szabó, G., Szûcs, A., Erõss, L., and Halász, P. (2001). Rhythmic hippocampal slow oscillation characterizes REM sleep in humans. Hippocampus *11*, 747–753. 10.1002/hipo.1090.

39. Mao, D., Avila, E., Caziot, B., Laurens, J., Dickman, J.D., and Angelaki, D.E. (2021). Spatial modulation of hippocampal activity in freely moving macaques. Neuron *109*, 3521-3534.e6. 10.1016/j.neuron.2021.09.032.

40. Gulli, R.A., Duong, L.R., Corrigan, B.W., Doucet, G., Williams, S., Fusi, S., and Martinez-Trujillo, J.C. (2020). Context-dependent representations of objects and space in the primate hippocampus during virtual navigation. Nat. Neurosci. *23*, 103–112. 10.1038/s41593-019-0548-3.

41. Courellis, H.S., Nummela, S.U., Metke, M., Diehl, G.W., Bussell, R., Cauwenberghs, G., and Miller, C.T. (2019). Spatial encoding in primate hippocampus during free navigation. PLoS Biol. *17*, e3000546. 10.1371/journal.pbio.3000546.

42. Rolls, E.T. (1999). Spatial view cells and the representation of place in the primate hippocampus. Hippocampus.

43. Ringo, J.L., Sobotka, S., Diltz, M.D., and Bunce, C.M. (1994). Eye movements modulate activity in hippocampal, parahippocampal, and inferotemporal neurons. J. Neurophysiol. *71*, 1285–1288. 10.1152/jn.1994.71.3.1285.

44. Bausch, M., Niediek, J., Reber, T.P., Mackay, S., Boström, J., Elger, C.E., and Mormann, F. (2021). Concept neurons in the human medial temporal lobe flexibly represent abstract relations between concepts. Nat. Commun. *12*, 6164. 10.1038/s41467-021-26327-3.

45. Hussin, A.T., Leonard, T.K., and Hoffman, K.L. (2020). Sharp-wave ripple features in macaques depend on behavioral state and cell-type specific firing. Hippocampus *30*, 50–59. 10.1002/hipo.23046.

46. Skaggs, W.E., McNaughton, B.L., Permenter, M., Archibeque, M., Vogt, J., Amaral, D.G., and Barnes, C.A. (2007). EEG sharp waves and sparse ensemble unit activity in the macaque hippocampus. J. Neurophysiol. *98*, 898–910. 10.1152/jn.00401.2007.

47. Le Van Quyen, M., Bragin, A., Staba, R., Crépon, B., Wilson, C.L., and Engel, J. (2008). Cell type-specific firing during ripple oscillations in the hippocampal formation of humans. J. Neurosci. *28*, 6104–6110. 10.1523/JNEUROSCI.0437-08.2008.

48. Katz, C.N., Schjetnan, A.G.P., Patel, K., Barkley, V., Hoffman, K.L., Kalia, S.K., Duncan, K.D., and Valiante, T.A. (2022). A corollary discharge mediates saccade-related inhibition of single units in mnemonic structures of the human brain. Curr. Biol. *32*, 3082-3094.e4. 10.1016/j.cub.2022.06.015.

49. Ison, M.J., Mormann, F., Cerf, M., Koch, C., Fried, I., and Quiroga, R.Q. (2011). Selectivity of pyramidal cells and interneurons in the human medial temporal lobe. J. Neurophysiol. *106*, 1713–1721. 10.1152/jn.00576.2010.

50. Liu, A.A., Henin, S., Abbaspoor, S., Bragin, A., Buffalo, E.A., Farrell, J.S., Foster, D.J., Frank, L.M., Gedankien, T., Gotman, J., et al. (2022). A consensus statement on detection of hippocampal sharp wave ripples and differentiation from other fast oscillations. Nat. Commun. *13*, 6000. 10.1038/s41467-022-33536-x.

821 51. Lee, E.K., Balasubramanian, H., Tsolias, A., Anakwe, S.U., Medalla, M., Shenoy, K.V., and
822 Chandrasekaran, C. (2021). Non-linear dimensionality reduction on extracellular waveforms
823 reveals cell type diversity in premotor cortex. eLife *10*. 10.7554/eLife.67490.

824 52. Trainito, C., von Nicolai, C., Miller, E.K., and Siegel, M. (2019). Extracellular spike waveform
825 dissociates four functionally distinct cell classes in primate cortex. Curr. Biol. *29*, 2973-2982.e5.
826 10.1016/j.cub.2019.07.051.

827 53. Csicsvari, J., Hirase, H., Czurkó, A., Mamiya, A., and Buzsáki, G. (1999). Oscillatory coupling of
828 hippocampal pyramidal cells and interneurons in the behaving Rat. J. Neurosci. *19*, 274–287.
829 10.1523/JNEUROSCI.19-01-00274.1999.

830 54. Ranck, J.B. (1973). Studies on single neurons in dorsal hippocampal formation and septum in
831 unrestrained rats. I. Behavioral correlates and firing repertoires. Exp. Neurol. *41*, 461–531.
832 10.1016/0014-4886(73)90290-2.

833 55. Holt, G.R., Softky, W.R., Koch, C., and Douglas, R.J. (1996). Comparison of discharge variability in
834 vitro and in vivo in cat visual cortex neurons. J. Neurophysiol. *75*, 1806–1814.
835 10.1152/jn.1996.75.5.1806.

836 56. Bezaire, M.J., and Soltesz, I. (2013). Quantitative assessment of CA1 local circuits: knowledge
837 base for interneuron-pyramidal cell connectivity. Hippocampus *23*, 751–785.
838 10.1002/hipo.22141.

839 57. Henze, D.A., Borhegyi, Z., Csicsvari, J., Mamiya, A., Harris, K.D., and Buzsáki, G. (2000).
840 Intracellular features predicted by extracellular recordings in the hippocampus in vivo. J.
841 Neurophysiol. *84*, 390–400. 10.1152/jn.2000.84.1.390.

842 58. Buzsáki, G., Anastassiou, C.A., and Koch, C. (2012). The origin of extracellular fields and currents--
843 EEG, ECoG, LFP and spikes. Nat. Rev. Neurosci. *13*, 407–420. 10.1038/nrn3241.

844 59. Jutras, M.J., Fries, P., and Buffalo, E.A. (2013). Oscillatory activity in the monkey hippocampus
845 during visual exploration and memory formation. Proc Natl Acad Sci USA *110*, 13144–13149.
846 10.1073/pnas.1302351110.

847 60. Hoffman, K.L., Dragan, M.C., Leonard, T.K., Micheli, C., Montefusco-Siegmund, R., and Valiante,
848 T.A. (2013). Saccades during visual exploration align hippocampal 3-8 Hz rhythms in human and
849 non-human primates. Front. Syst. Neurosci. *7*, 43. 10.3389/fnsys.2013.00043.

850 61. Brincat, S.L., and Miller, E.K. (2015). Frequency-specific hippocampal-prefrontal interactions
851 during associative learning. Nat. Neurosci. *18*, 576–581. 10.1038/nn.3954.

852 62. Hussin, A.T., Abbaspoor, S., and Hoffman, K.L. (2022). Retrosplenial and Hippocampal Synchrony
853 during Retrieval of Old Memories in Macaques. J. Neurosci. *42*, 7947–7956.
854 10.1523/JNEUROSCI.0001-22.2022.

855 63. Allen, T.A., Salz, D.M., McKenzie, S., and Fortin, N.J. (2016). Nonspatial sequence coding in CA1
856 neurons. J. Neurosci. *36*, 1547–1563. 10.1523/JNEUROSCI.2874-15.2016.

857 64. Jayachandran, M., Viena, T.D., Garcia, A., Veliz, A.V., Leyva, S., Roldan, V., Vertes, R.P., and Allen,
858 T.A. (2023). Nucleus reuniens transiently synchronizes memory networks at beta frequencies.
859 Nat. Commun. *14*, 4326. 10.1038/s41467-023-40044-z.

860 65. Lansink, C.S., Meijer, G.T., Lankelma, J.V., Vinck, M.A., Jackson, J.C., and Pennartz, C.M.A. (2016).
861 Reward Expectancy Strengthens CA1 Theta and Beta Band Synchronization and Hippocampal-
862 Ventral Striatal Coupling. J. Neurosci. *36*, 10598–10610. 10.1523/JNEUROSCI.0682-16.2016.

863 66. Buzsáki, G. (2015). Hippocampal sharp wave-ripple: A cognitive biomarker for episodic memory
864 and planning. Hippocampus *25*, 1073–1188. 10.1002/hipo.22488.

865 67. Viney, T.J., Lasztoczi, B., Katona, L., Crump, M.G., Tukker, J.J., Klausberger, T., and Somogyi, P.
866 (2013). Network state-dependent inhibition of identified hippocampal CA3 axo-axonic cells in
867 vivo. Nat. Neurosci. *16*, 1802–1811. 10.1038/nn.3550.

868 68. Dudok, B., Szoboszlay, M., Paul, A., Klein, P.M., Liao, Z., Hwaun, E., Szabo, G.G., Geiller, T.,
869 Vancura, B., Wang, B.-S., et al. (2021). Recruitment and inhibitory action of hippocampal axo-
870 axonic cells during behavior. Neuron *109*, 3838-3850.e8. 10.1016/j.neuron.2021.09.033.

871 69. Szabo, G.G., Farrell, J.S., Dudok, B., Hou, W.-H., Ortiz, A.L., Varga, C., Moolchand, P., Gulsever,
872 C.I., Gschwind, T., Dimidschstein, J., et al. (2022). Ripple-selective GABAergic projection cells in
873 the hippocampus. Neuron *110*, 1959-1977.e9. 10.1016/j.neuron.2022.04.002.

874 70. Amilhon, B., Huh, C.Y.L., Manseau, F., Ducharme, G., Nichol, H., Adamantidis, A., and Williams, S.
875 (2015). Parvalbumin interneurons of hippocampus tune population activity at theta frequency.
876 Neuron *86*, 1277–1289. 10.1016/j.neuron.2015.05.027.

877 71. Ognjanovski, N., Schaeffer, S., Wu, J., Mofakham, S., Maruyama, D., Zochowski, M., and Aton, S.J.
878 (2017). Parvalbumin-expressing interneurons coordinate hippocampal network dynamics
879 required for memory consolidation. Nat. Commun. *8*, 15039. 10.1038/ncomms15039.

880 72. Raven, F., and Aton, S.J. (2021). The Engram's Dark Horse: How Interneurons Regulate State-
881 Dependent Memory Processing and Plasticity. Front. Neural Circuits *15*, 750541.
882 10.3389/fncir.2021.750541.

883 73. Xia, F., Richards, B.A., Tran, M.M., Josselyn, S.A., Takehara-Nishiuchi, K., and Frankland, P.W.
884 (2017). Parvalbumin-positive interneurons mediate neocortical-hippocampal interactions that
885 are necessary for memory consolidation. eLife *6*. 10.7554/eLife.27868.

886 74. Bugeon, S., Duffield, J., Dipoppa, M., Ritoux, A., Prankerd, I., Nicoloutsopoulos, D., Orme, D.,
887 Shinn, M., Peng, H., Forrest, H., et al. (2022). A transcriptomic axis predicts state modulation of
888 cortical interneurons. Nature *607*, 330–338. 10.1038/s41586-022-04915-7.

889 75. Schneider, A., Azabou, M., McDougall-Vigier, L., Parks, D.F., Ensley, S., Bhaskaran-Nair, K.,
890 Nowakowski, T., Dyer, E.L., and Hengen, K.B. (2023). Transcriptomic cell type structures in vivo
891 neuronal activity across multiple timescales. Cell Rep. *42*, 112318. 10.1016/j.celrep.2023.112318.

892 76. Royer, S., Zemelman, B.V., Losonczy, A., Kim, J., Chance, F., Magee, J.C., and Buzsáki, G. (2012).
893 Control of timing, rate and bursts of hippocampal place cells by dendritic and somatic inhibition.
894 Nat. Neurosci. *15*, 769–775. 10.1038/nn.3077.

77. English, D.F., McKenzie, S., Evans, T., Kim, K., Yoon, E., and Buzsáki, G. (2017). Pyramidal Cell-Interneuron Circuit Architecture and Dynamics in Hippocampal Networks. Neuron *96*, 505-520.e7. 10.1016/j.neuron.2017.09.033.

78. Lapray, D., Lasztoczi, B., Lagler, M., Viney, T.J., Katona, L., Valenti, O., Hartwich, K., Borhegyi, Z., Somogyi, P., and Klausberger, T. (2012). Behavior-dependent specialization of identified hippocampal interneurons. Nat. Neurosci. *15*, 1265–1271. 10.1038/nn.3176.

79. Krook-Magnuson, E., Varga, C., Lee, S.-H., and Soltesz, I. (2012). New dimensions of interneuronal specialization unmasked by principal cell heterogeneity. Trends Neurosci. *35*, 175–184. 10.1016/j.tins.2011.10.005.

80. Soltesz, I., and Losonczy, A. (2018). CA1 pyramidal cell diversity enabling parallel information processing in the hippocampus. Nat. Neurosci. *21*, 484–493. 10.1038/s41593-018-0118-0.

81. Barbas, H., and Blatt, G.J. (1995). Topographically specific hippocampal projections target functionally distinct prefrontal areas in the rhesus monkey. Hippocampus *5*, 511–533. 10.1002/hipo.450050604.

82. Insausti, R., and Muñoz, M. (2001). Cortical projections of the non-entorhinal hippocampal formation in the cynomolgus monkey (Macaca fascicularis). Eur. J. Neurosci. *14*, 435–451. 10.1046/j.0953-816x.2001.01662.x.

83. Stark, E., Roux, L., Eichler, R., Senzai, Y., Royer, S., and Buzsáki, G. (2014). Pyramidal cell-interneuron interactions underlie hippocampal ripple oscillations. Neuron *83*, 467–480. 10.1016/j.neuron.2014.06.023.

84. Berndt, M., Trusel, M., Roberts, T.F., Pfeiffer, B.E., and Volk, L.J. (2023). Bidirectional synaptic changes in deep and superficial hippocampal neurons following in vivo activity. Neuron *111*, 2984-2994.e4. 10.1016/j.neuron.2023.08.014.

85. Donoghue, T., Haller, M., Peterson, E.J., Varma, P., Sebastian, P., Gao, R., Noto, T., Lara, A.H., Wallis, J.D., Knight, R.T., et al. (2020). Parameterizing neural power spectra into periodic and aperiodic components. Nat. Neurosci. *23*, 1655–1665. 10.1038/s41593-020-00744-x.

86. Chen, Y.Y., Yoshor, D., Sheth, S.A., and Foster, B.L. (2020). Stability of ripple events during task engagement in human hippocampus. BioRxiv. 10.1101/2020.10.17.342881.

87. Pachitariu, M., Steinmetz, N., Kadir, S., Carandini, M., and Harris, K.D. (2016). Kilosort: realtime spike-sorting for extracellular electrophysiology with hundreds of channels. BioRxiv. 10.1101/061481.

88. Lecoq, J., Oliver, M., Siegle, J.H., Orlova, N., Ledochowitsch, P., and Koch, C. (2021). Removing independent noise in systems neuroscience data using DeepInterpolation. Nat. Methods *18*, 1401–1408. 10.1038/s41592-021-01285-2.

89. Sullivan, D., Csicsvari, J., Mizuseki, K., Montgomery, S., Diba, K., and Buzsáki, G. (2011). Relationships between hippocampal sharp waves, ripples, and fast gamma oscillation: influence of dentate and entorhinal cortical activity. J. Neurosci. *31*, 8605–8616. 10.1523/JNEUROSCI.0294-11.2011.

90. Mitzdorf, U. (1985). Current source-density method and application in cat cerebral cortex: investigation of evoked potentials and EEG phenomena. Physiol. Rev. *65*, 37–100. 10.1152/physrev.1985.65.1.37.

91. Tenke, C.E., Schroeder, C.E., Arezzo, J.C., and Vaughan, H.G. (1993). Interpretation of high-resolution current source density profiles: a simulation of sublaminar contributions to the visual evoked potential. Exp. Brain Res. *94*, 183–192. 10.1007/BF00230286.

92. Steinschneider, M., Tenke, C.E., Schroeder, C.E., Javitt, D.C., Simpson, G.V., Arezzo, J.C., and Vaughan, H.G. (1992). Cellular generators of the cortical auditory evoked potential initial component. Electroencephalogr. Clin. Neurophysiol. *84*, 196–200. 10.1016/0168-5597(92)90026-8.

93. McInnes, L., Healy, J., and Melville, J. (2018). UMAP: Uniform Manifold Approximation and Projection for Dimension Reduction. arXiv. 10.48550/arxiv.1802.03426.

94. Petersen, P.C., Siegle, J.H., Steinmetz, N.A., Mahallati, S., and Buzsáki, G. (2021). CellExplorer: A framework for visualizing and characterizing single neurons. Neuron *109*, 3594-3608.e2. 10.1016/j.neuron.2021.09.002.

95. Vinck, M., van Wingerden, M., Womelsdorf, T., Fries, P., and Pennartz, C.M.A. (2010). The pairwise phase consistency: a bias-free measure of rhythmic neuronal synchronization. Neuroimage *51*, 112–122. 10.1016/j.neuroimage.2010.01.073.

96. Berens, P. (2009). circstat : a *MATLAB* toolbox for circular statistics. J. Stat. Softw. *31*. 10.18637/jss.v031.i10.

97. Stark, E., and Abeles, M. (2009). Unbiased estimation of precise temporal correlations between spike trains. J. Neurosci. Methods *179*, 90–100. 10.1016/j.jneumeth.2008.12.029.

98. Nádasdy, Z., Hirase, H., Czurkó, A., Csicsvari, J., and Buzsáki, G. (1999). Replay and time compression of recurring spike sequences in the hippocampus. J. Neurosci. *19*, 9497–9507. 10.1523/JNEUROSCI.19-21-09497.1999.

99. Blair, R.C., and Karniski, W. (1993). An alternative method for significance testing of waveform difference potentials. Psychophysiology *30*, 518–524. 10.1111/j.1469-8986.1993.tb02075.x.

100. Lopes-dos-Santos, V., Conde-Ocazionez, S., Nicolelis, M.A.L., Ribeiro, S.T., and Tort, A.B.L. (2011). Neuronal assembly detection and cell membership specification by principal component analysis. PLoS ONE *6*, e20996. 10.1371/journal.pone.0020996.

101. Lopes-dos-Santos, V., Ribeiro, S., and Tort, A.B.L. (2013). Detecting cell assemblies in large neuronal populations. J. Neurosci. Methods *220*, 149–166. 10.1016/j.jneumeth.2013.04.010.

102. van de Ven, G.M., Trouche, S., McNamara, C.G., Allen, K., and Dupret, D. (2016). Hippocampal Offline Reactivation Consolidates Recently Formed Cell Assembly Patterns during Sharp Wave-Ripples. Neuron *92*, 968–974. 10.1016/j.neuron.2016.10.020.

103. Peyrache, A., Benchenane, K., Khamassi, M., Wiener, S.I., and Battaglia, F.P. (2010). Principal component analysis of ensemble recordings reveals cell assemblies at high temporal resolution. J. Comput. Neurosci. *29*, 309–325. 10.1007/s10827-009-0154-6.

104. Boucly, C.J., Pompili, M.N., Todorova, R., Leroux, E.M., Wiener, S., and Zugaro, M. (2022). Flexible communication between cell assemblies and “reader” neurons. BioRxiv. 10.1101/2022.09.06.506754.

105. Maris, E., and Oostenveld, R. (2007). Nonparametric statistical testing of EEG- and MEG-data. J. Neurosci. Methods *164*, 177–190. 10.1016/j.jneumeth.2007.03.024.

106. Gondan, M. (2010). A permutation test for the race model inequality. Behav. Res. Methods *42*, 23–28. 10.3758/BRM.42.1.23.

107. Groppe, D.M., Urbach, T.P., and Kutas, M. (2011). Mass univariate analysis of event-related brain potentials/fields I: a critical tutorial review. Psychophysiology *48*, 1711–1725. 10.1111/j.1469-8986.2011.01273.x.

108. Groppe, D.M., Urbach, T.P., and Kutas, M. (2011). Mass univariate analysis of event-related brain potentials/fields II: Simulation studies. Psychophysiology *48*, 1726–1737. 10.1111/j.1469-8986.2011.01272.x.